Stable Discrete Bending by Analytic Eigensystem and Adaptive Orthotropic Geometric Stiffness

ZHENDONG WANG, Style3D Research, China
YIN YANG, The University of Utah, USA and Style3D Research, China
HUAMIN WANG, Style3D Research, China

(a) BMR: x16 (b) BMR: x8 (c) BMR: x4 (d) BMR: x2 (e) BMR: x1

(f) BMR: x16 (g) BMR: x8 (h) BMR: x4 (i) BMR: x2 (j) BMR: x1

Fig. 1. We illustrate the effectiveness of our approach with a T-shirt example. In the first row, we simulate the same T-shirt using five different scuba fabrics, each with the same high bending stiffness but different membrane stiffness. From (a) to (e), the lower the ratio of bending stiffness to membrane stiffness (BMR), the higher the membrane stiffness. In the second row, we use five different fabrics with the same small membrane stiffness but varying bending stiffness properties. From (f) to (j), the lower the BMR, the lower the bending stiffness. Note that figures (a) and (f) use the same scuba fabric with high bending stiffness and small membrane stiffness. Our proposed method allows for the stable simulation of fabrics with a wide range of BMRs. (BMR x1 corresponds to a Kirchhoff-Love thin plate with a thickness of 1 mm. Given a BMR xN, the corresponding thickness is $\sqrt{N}$ mm. For example, BMR x16 corresponds to 4 mm.)

In this paper, we address two limitations of dihedral angle based discrete bending (DAB) models, i.e. the indefiniteness of their energy Hessian and their vulnerability to geometry degeneracies. To tackle the indefiniteness issue, we present novel analytic expressions for the eigensystem of a DAB energy Hessian. Our expressions reveal that DAB models typically have positive, negative, and zero eigenvalues, with four of each, respectively. By using these expressions, we can efficiently project an indefinite DAB energy Hessian as positive semi-definite analytically. To enhance the stability of DAB models at degenerate geometries, we propose rectifying their indefinite geometric stiffness matrix by using orthotropic geometric stiffness matrices with adaptive parameters calculated from our analytic eigensystem. Among the twelve motion modes of a dihedral element, our resulting Hessian for DAB models retains only the desirable bending modes, compared to the undesirable altitude-changing modes of the exact Hessian with original geometric stiffness, all modes of the Gauss-Newton approximation without geometric stiffness, and no modes of the projected Hessians with inappropriate geometric stiffness. Additionally, we suggest adjusting the compression stiffness according to the Kirchhoff-Love thin plate theory to

Authors' addresses: Zhendong Wang, Style3D Research, China, wang.zhendong.619@gmail.com; Yin Yang, The University of Utah, USA and Style3D Research, China, yin.yang@utah.edu; Huamin Wang, Style3D Research, China, wanghmin@gmail.com.

0730-0301/2023/12-ART183 $15.00
https://doi.org/10.1145/3618372

avoid over-compression. Our method not only ensures the positive semi-definiteness but also avoids instability caused by large bending forces at degenerate geometries. To demonstrate the benefit of our approaches, we show comparisons against existing methods on the simulation of cloth and thin plates in challenging examples.

CCS Concepts: • **Computing methodologies → Physical Simulation**; **Modeling Methodologies**.

Additional Key Words and Phrases: discrete bending, dihedral angle, eigensystem, geometric stiffness

ACM Reference Format:
Zhendong Wang, Yin Yang, and Huamin Wang. 2023. Stable Discrete Bending by Analytic Eigensystem and Adaptive Orthotropic Geometric Stiffness. *ACM Trans. Graph.* 42, 6, Article 183 (December 2023), 16 pages. https://doi.org/10.1145/3618372

1 INTRODUCTION

Physics-based simulation of cloth and thin plates are widely used in industrial fashion design and animation movies to create realistic folds and wrinkles. The formation of these folds and wrinkles depends on constitutive models for bending deformation. While elasticity models have received a lot of attention in the graphics community and are constantly advancing, bending models have progressed slowly since their boom in the early 21st century.

Dihedral angle based discrete bending (DAB) models have been widely used in the simulation of cloth, thin plates, and thin shells. However, the two main limitations of using dihedral angles, as pointed out by Tamstorf and Grinspun [2013], have been overlooked for a long time. First, the Hessian of a dihedral angle, also the geometric stiffness matrix, is indefinite, as demonstrated in Section. 4.1. This indefiniteness is due to the non-linearity and non-convexity of a dihedral angle with respect to positions. Second, geometry degeneracies, such as edge degeneration and altitude collapse, make the computation of bending forces and Hessian vulnerable to divergence, leading to instability of simulation, especially when bending stiffness dominates membrane stiffness and large bending forces can instantaneously over-stretch or over-compress triangles. Existing methods typically assume triangle meshes undergoing (near-) isometric deformation, where strong enough membrane stiffness can effectively act as geometric stiffness for DAB models. As a result, the impact of an indefinite bending energy Hessian on simulation stability is negligible [Grinspun et al. 2003; Tamstorf and Grinspun 2013], and approximations can be employed to simplify the computation of DAB models [Bergou et al. 2006b; Bridson et al. 2003]. Moreover, degenerate geometries are no longer problems in (near-) isometric simulations.

However, this assumption is not universally valid in industrial interactive applications, where users should possess the autonomy to adjust membrane and bending stiffness independently, thereby achieving desired simulation effects without being constrained by realistic material limitations. While simulation stability can be attained through nonlinear methods with small step lengths, in industrial contexts, it is often advantageous to employ a sole iteration of Newton's method accompanied by a limited number of PCG iterations as the linear solver [Baraff and Witkin 1998; Tournier et al. 2015; Wu et al. 2022]. For instance, in real-time interactive fashion design, this strategy strikes a balance between interactive performance and robustness without expensive step-length line-searching. Therefore, the instability concerns for DAB models become significant, particularly when bending stiffness dominates membrane stiffness for special visual effects. While a high bending-membrane ratio (BMR) is uncommon in the realm of realistic continuum materials, it can readily manifest in specialized composite materials. As displayed in Fig. 1, certain scuba fabrics [Yip and Ng 2008; Zhang et al. 2020] exhibit high BMRs with fabric thickness up to $4 \sim 7.5$ mm. To ensure both interactive robustness and user-friendliness, it is imperative to refrain from constraining the range of permissible BMRs and uphold the simulation stability across a broad range of BMRs.

Existing methods for restoring the positive semi-definiteness of FEM elastic energy Hessian [Smith et al. 2019; Teran et al. 2005] are not applicable to DAB models. Singular value decomposition (SVD) can be used to restore the positive semi-definiteness of an energy Hessian, but it is computationally expensive and suffers potential numerical instability. To address indefiniteness, we present novel analytic expressions for the eigensystem of DAB models. Our method reveals that DAB models typically have positive, negative, and zero eigenvalues, with four of each, when a dihedral element is away from its reference state. Therefore, negative eigenvalues can be clamped to zero using our analytic expressions, which is more efficient and stable than using SVD. Our eigenanalysis is based on a concise matrix expression for the dihedral angle Hessian, which serves as the geometric stiffness of a dihedral element. This expression reveals that only the undesirable altitude-changing modes of a dihedral element are retained under the effect of the geometric stiffness. Furthermore, we observe that the Hessian projection cannot promise stability in only one Newton's iteration when the BMR is high, as it eliminates all motion modes of a dihedral element. To enhance stability at degenerate geometries, we propose applying orthotropic geometric stiffness with adaptive parameters. This approach retains only the desirable bending modes and effectively suppress instantaneous over-stretching and over-compression caused by large bending forces. Since we leave bending forces unmodified, over-compression is inevitable where bending forces dominate membrane forces. We notice that thin materials are difficult to compress in plane if buckling is prevented, regardless of their ease of stretching. Therefore, we suggest adjusting the local compression stiffness of each triangle element according to the Kirchhoff-Love thin plate theory to avoid degenerate geometries. Because it is an adaptive adjustment based on the strain of each triangle, the resulting compression stiffness maintains $C1$ continuity near the reference state, facilitating smooth transitions between in-plane compression and stretching. To be summarized, our main contributions include:

- we provide a concise derivation of the dihedral angle Hessian and present novel analytic expressions for the eigensystem of DAB models. This enables us to restore the positive semi-definiteness of the energy Hessian efficiently;
- we propose an orthotropic geometric stiffness model with parameters determined by the analytic eigensystems to enhance the simulation stability at degenerate geometries;
- we suggest adjusting the compression stiffness based on the Kirchhoff-Love thin plate theory to handle triangle over-compression and avoid geometry degeneracies.

Overall, our contributions improve the stability of DAB models and enable them to handle a wide range of materials in linearized simulation with only one Newton's iteration without a line search, making them more useful for industrial interactive fashion design and animation movies.

2 RELATED WORK

In physics-based simulations, bending models are essential for accurately representing the appearance of thin materials modeled by discrete surfaces. These models typically rely on geometric curvatures that play important roles in both geometric and physical modeling [Grinspun et al. 2003; Sullivan 2005, 2008]. Meyer et al. [2003] presented a method to evaluate discrete mean curvature and Laplace-Beltrami for triangulated 2-manifolds. Based on restricted Delaunay triangulation and normal cycle, Cohen-Steiner and Morvan [2003] defined several discrete curvature measures. Different discrete elements lead to different curvature measures, including vertex-based and edge-based curvature measures [Polthier et al. 2002], as well as triangle-based shape operators [Gingold et al. 2004; Grinspun et al. 2006]. Related reviews can be found in [Grinspun 2006; Wacker and Thomaszewski 2006]. Meanwhile, the general form of curvature-based surface energy has been presented in [Bobenko and Schröder 2005; Canham 1970; Helfrich 1973], with the bending energy of discrete surfaces being one type of curvature-based surface energy.

To model bending effects of thin materials, one approach is to employ the Kirchhoff-Love continuum theory, which assumes that the shell does not experience any transverse shear and the normal is always orthogonal to the mid-surface. However, to maintain bending continuity between discrete elements, computationally expensive techniques such as high-order [Rank et al. 2005; Rémillard and Kry 2013] or subdivision finite elements [Green et al. 2002; Guo et al. 2018] are typically required. Alternatively, one can use piecewise linear finite elements and model bending energy on dihedral elements. In this paper, we specifically focus on the discrete bending model defined on linear finite elements, which is widely used in physics-based simulation. For a discrete dihedral element, the bending energy is built on dihedral angle based discrete edge-based curvature. Baraff and Witkin [1998] introduced a bending constraint that restricts the dihedral angle of an edge to model the bending behaviors of clothing. Grinspun et al. [2003] defined the bending energy of discrete shells from the perspective of mean curvature difference, based on the conclusion of [Cohen-Steiner and Morvan 2003]. Bridson et al. [2003] directly generated bending forces for a dihedral element, with a magnitude of the cosine of half the dihedral angle and well-designed directions that are actually the gradient of a dihedral angle. They also imposed explicit damping forces to enhance stability. To embed bending energy in the framework of implicit time integration, the complicated gradient and Hessian of a dihedral angle are needed. Fortunately, they have been presented in detail by Tamstorf and Grinspun [2013]. Based on these hinge-based bending models, fantastic applications [Bergou et al. 2007; Chen et al. 2018, 2021; Grinspun 2005; Narain et al. 2013] have appeared, and estimation and measurement methods for bending parameters [Feng et al. 2022; Romero et al. 2021; Wang et al. 2011] have been proposed. For efficiency, approximated bending models [Bergou et al. 2006a,b; Garg et al. 2007; Volino and Magnenat-Thalmann 2006] utilize linearized edge-based mean curvatures to obtain a constant energy Hessian. *Quadratic Bending* proposed by Bergou et al. [2006b] achieves a constant positive semi-definite Hessian but can only retain physical accuracy in the case of flat dihedral angles at rest and small in-plane deformations. Though positive semi-definiteness of DAB models with a quadratic bending energy can be guaranteed by the Gauss-Newton method which omits the indefinite dihedral angle Hessian, lack of geometric stiffness can lead to instability in the case of high bending-membrane ratios and degenerate geometries.

Geometric stiffness arises from the geometric non-linearity of strain with respect to positions. It has been generally employed in buckling analysis, and interested readers can refer to [Cook 1994; Zienkiewicz et al. 2000] for more details. In the simulation of solid mechanics, geometric stiffness plays a crucial role in maintaining the stability of elasticity and contacts. When using springs to enforce two-point distance constraints, the linear processing of spring forces in the transverse direction can lead to instabilities in contact scenarios [Kaufman et al. 2014] and cloth simulation [Goldenthal et al. 2007]. To address this transverse instability of stiff springs, instead of resorting to nonlinear methods, Tournier et al. [2015] developed a first-degree method that requires only one linear solution by utilizing the geometric stiffness of constraint forces to ensure stability. Andrews et al. [2017] also utilized geometric stiffness to enhance the stability of simulations of articulated rigid bodies.

However, few studies have focus on the instability issue of dihedral angle based bending models. While significant progress has been made in enhancing the stability of elasticity models, including spring-based methods [Choi and Ko 2002; Tournier et al. 2015] and FEM-based methods [Smith et al. 2018, 2019; Teran et al. 2005], there is a gap in addressing stability concerns in discrete bending models. In this work, we aim to fill the gap by providing analytic expressions for their eigensystem and replacing the indefinite geometric stiffness matrix with positive semi-definite orthotropic geometric stiffness matrices.

3 BACKGROUND

Before diving into the investigation of existing and our approaches for stabilizing discrete bending models, we would like to provide a brief introduction to their background. In this paper, we use unbolded characters in lowercase (a) or uppercase (A) to denote scalars, bolded lowercase (**a**) for column vectors, and bolded uppercase (**A**) for matrices. A bar means a reference value. ⊗ represents the Kronecker product. The definition of frequently used symbols can be found in Table. 1.

3.1 DAB Models

A dihedral element is composed of four vertices $\mathbf{x}_i \in \mathbb{R}^3 (i \in \{0, 1, 2, 3\})$ and two adjacent triangles that share a common hinge edge, as shown in Fig. 2(a). Its reference area is $\bar{A}/3$, which is one-third of the reference triangle area sum $\bar{A}$, and the rest length of the hinge edge is $\bar{l}$. A general bending energy on the element can be defined w.r.t. the packed position $\mathbf{x} = [\mathbf{x}_0^\top, \mathbf{x}_1^\top, \mathbf{x}_2^\top, \mathbf{x}_3^\top]^\top \in \mathbb{R}^{12}$ as

$$\Psi(\mathbf{x}) = \mu \, \psi(\theta, \bar{\theta}), \tag{1}$$

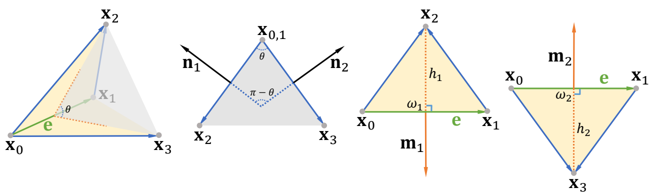

(a) Dihedral element (b) Normals (c) Altitudes and barycentric weights

Fig. 2. (a) A dihedral element with dihedral angle θ smaller than π consist of a hinge edge and two adjacent triangles. The hinge edge has length l and normalized direction $\mathbf{e}$. (b) The angle between the two normalized triangle normals $\mathbf{n}_1$ and $\mathbf{n}_2$ is $\pi-\theta$. (c) The hinge altitudes on the two triangles are h_1 and h_2 respectively. $\mathbf{m}_1$ and $\mathbf{m}_2$ are the normalized altitude vectors. When projecting the two off-edge vertices $\mathbf{x}_2$ and $\mathbf{x}_3$ on the hinge edge, the barycentric weights of their projection points are respectively ω_1 and ω_2.

where θ and $\bar{\theta}$ are the deformed and reference dihedral angles, and $\mu = 3\bar{l}^2/\bar{A}$ is a reference shape factor. Different choices of $\psi(\theta,\bar{\theta})$ result in several bending models:

- $\psi(\theta,\bar{\theta}) = \frac{1}{2}(\theta-\bar{\theta})^2$: referred to as *Discrete Shells* [Grinspun et al. 2003];
- $\psi(\theta,\bar{\theta}) = 2(\sin\frac{\theta-\bar{\theta}}{2})^2$: referred to as *Cubic Shells* [Garg et al. 2007] whose energy is cubic for unstretched surfaces;
- $\psi(\theta,\bar{\theta}) = 2(\cos\frac{\theta}{2})^2$: referred to as *Discrete Willmore Energy* [Wardetzky et al. 2007]. It is equivalent to *Quadratic Bending* [Bergou et al. 2006b] for inextensible surfaces;
- $\psi(\theta,\bar{\theta}) = \cos\frac{\bar{\theta}}{2}\theta - 2\sin\frac{\theta}{2}$: proposed by Bridson et al. [2003] for the simulation of clothing with folds and wrinkles and referred to as *Bridson's model* in this paper;
- $\psi(\theta,\bar{\theta}) = 2(\cot\frac{\theta}{2} - \cot\frac{\bar{\theta}}{2})^2$: proposed by Tamstorf and Grinspun [2013] to avoid penetrations and referred to as *Tamstorf's model* in this paper.

Recently, some studies [Romero et al. 2021] have emphasized the importance of considering $\theta-\bar{\theta}$ rather than θ or $\bar{\theta}$ individually for simulation results being consistent with physical reality. To integrate these models into implicit time integration, expressions of bending force and energy Hessian are required,

$$\mathbf{f} = -\mu g \nabla_{\mathbf{x}}\theta \quad \textit{and} \quad \mathbf{H} = \mu\left(p\mathbf{P} + g\mathbf{G}\right), \tag{2}$$

in which $g = \frac{\partial\psi}{\partial\theta}$ and $p = \frac{\partial^2\psi}{\partial\theta^2}$, $\nabla_{\mathbf{x}}\theta \in \mathbb{R}^{12}$ (Eq. 3) is the dihedral angle gradient, $\mathbf{G} = \frac{\partial^2\theta}{\partial\mathbf{x}^2} \in \mathbb{R}^{12\times12}$ (Eq. 4) is the dihedral angle Hessian and $\mathbf{P} = \frac{\partial\theta}{\partial\mathbf{x}}^{\mathsf{T}}\frac{\partial\theta}{\partial\mathbf{x}} \in \mathbb{R}^{12\times12}$ is a positive semi-definite projection matrix that projects a vector onto the subspace spanned by the dihedral angle gradient. Tamstorf and Grinspun [2013] conducted a thorough analysis of the calculation of these terms. However, their derivation and Hessian expressions are cumbersome. To facilitate the analysis of the instability of DAB models, we present a more concise matrix expression for the Hessian of a dihedral angle in Section. 4.1.

Table 1. Frequently used symbols. The definition of some symbols can be found in Fig. 2.

Symbol	Meaning	Symbol	Meaning
θ	dihedral angle	$\mathbf{n}_1, \mathbf{n}_2$	triangle normals
l	hinge edge length	$\mathbf{m}_1, \mathbf{m}_2$	altitude vectors
h_1, h_2	hinge altitudes	$\mathbf{e}$	hinge edge vector
ω_1, ω_2	barycentric coords	$\mathbf{y}_1, \mathbf{y}_2$	$\sum \mathbf{t}_1[i]\Delta\mathbf{x}_i$, $\sum \mathbf{t}_2[i]\Delta\mathbf{x}_i$
ψ	energy density	$\mathbf{y}_3$	$\sum \mathbf{s}[i]\Delta\mathbf{x}_i$
h	thickness	$\mathbf{s}$	$l^{-1}[1,-1,0,0]^{\mathsf{T}}$
g	$\frac{\partial\psi}{\partial\theta}$	$\mathbf{t}_1$	$h_1^{-1}[\omega_1-1,-\omega_1,1,0]^{\mathsf{T}}$
p	$\frac{\partial^2\psi}{\partial\theta^2}$	$\mathbf{t}_2$	$h_2^{-1}[\omega_2-1,-\omega_2,0,1]^{\mathsf{T}}$
μ	$3\bar{l}/\bar{A}$	$\mathbf{f}$	bending force
A	area sum	$\mathbf{H}$	energy Hessian
α	damping params	$\mathbf{G}$	dihedral angle Hessian
Y	Young's modulus	$\mathbf{P}$	$\nabla_{\mathbf{x}}\theta$'s projection matrix

3.2 Problems

Tamstorf and Grinspun [2013] identified two primary limitations of DAB models: the indefiniteness of a dihedral angle Hessian and the vulnerability to geometry degeneracies.

3.2.1 Indefiniteness. If a dihedral element undergoes bending deformation, the bending forces and dihedral angle Hessian $\mathbf{G}$ will come into play due to $g \neq 0$. The presence of $\mathbf{G}$, whose indefiniteness will be demonstrated in Section. 4.1, may result in negative eigenvalues for the energy Hessian $\mathbf{H}$. In some DAB models, such as *Cubic Shells*, *Discrete Willmore Energy* and *Tamstorf's model*, negative eigenvalues can arise from a negative p when the dihedral angle difference is large. Our analytic eigensystem in Section. 4.2 demonstrates that $\mathbf{H}$ is indefinite when a dihedral element is away from its reference bending state. Using an indefinite bending Hessian in cloth or thin plate simulation could lead to instability at large bending deformations, as illustrated in Fig. 5(a).

The most common method to address the indefiniteness of an energy Hessians is to perform *Hessian Projection*, which involves clamping the negative eigenvalue to zero. Exact Hessian projection can only be performed numerically using SVD, which is not computationally efficient. More efficient methods, such as [Smith et al. 2019; Teran et al. 2005], use the deformation gradient of finite elements to obtain a block-diagonal intrinsic deformation matrix that can be efficiently projected as positive semi-definite. However, they cannot be applied to DAB models because it is impossible to define a deformation-gradient-like variable for dihedral elements.

3.2.2 Geometry Degeneracies. The computation of bending force and energy Hessian in DAB models involves dividing hinge edge length and altitudes, which can be problematic when edges become degenerate or altitudes collapse. Although divisions by zero can be numerically avoided, degenerate altitudes will produce large out-of-plane bending forces which can stretch or compress triangles excessively if the bending stiffness dominates the membrane stiffness. As illustrated in Fig. 8 and Fig. 10, geometry degeneracies occur at the corners where triangles are over-compressed by large bending forces. However, DAB models do not respond to in-plane

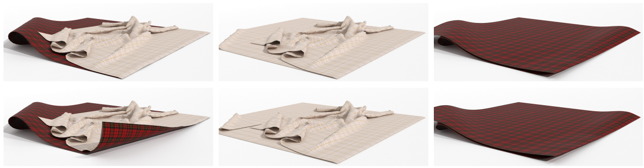

(a) Soft and Stiff (b) Both Soft (c) Both Stiff

Fig. 3. Cloth examples with two pieces stitched together. The red piece is stiff with high bending stiffness and the cream piece is soft with low bending stiffness. There is a large folding angle at the seam. Using dynamic in-plane variables produces plausible simulation results in the first row. In contrast, using constant in-plane variables produces an artifact at the seam in the second row of column (a).

deformations, which can affect the magnitude and direction of bending forces but have no influence on bending energies. While it may be acceptable to assume constant in-plane variables, e.g. h_1, h_2, ω_1, ω_2 and l, in an isometric simulation, doing so in a non-isometric simulation can lead to artifacts. Fig. 3 shows that assuming constant in-plane variables crimps the seam between soft and stiff cloth pieces due to non-conservative angular momentum, whereas using dynamic in-plane variables produces more plausible results.

4 OUR METHOD

To overcome the limitations of DAB models, we propose several novel techniques. First, we provide a compact matrix expression for the dihedral angle Hessian and a profound analysis for the geometric stiffness of DAB models. Second, we present an analytic eigensystem for the energy Hessian to address the indefiniteness issue. Third, we propose an adaptive orthotropic geometric stiffness model to improve the stability of DAB models. Finally, we suggest adjusting compression stiffness based on the Kirchhoff-Love plate theory to handle over-compression.

4.1 Dihedral Angle Hessian

In addition to the dihedral angle θ and hinge edge length l, we notice that the shape of a dihedral element is also influenced by four other pivotal variables: h_1 and h_2, altitudes on the hinge edge, and ω_1 and ω_2, barycentric weights of $\mathbf{x}_2$ and $\mathbf{x}_3$ on the hinge edge. By defining two vectors $\mathbf{t}_1 = h_1^{-1}[\omega_1-1, -\omega_1, 1, 0]^\top$ and $\mathbf{t}_2 = h_2^{-1}[\omega_2-1, -\omega_2, 0, 1]^\top$, the gradient of a dihedral angle can be expressed as a column vector in $\mathbb{R}^{12}$,

$$\nabla_{\mathbf{x}}\theta = \mathbf{t}_1 \otimes \mathbf{n}_1 + \mathbf{t}_2 \otimes \mathbf{n}_2, \tag{3}$$

where $\mathbf{n}_1$ and $\mathbf{n}_2$ are unit normals of the two adjacent triangles, as shown in Fig. 2(b). Their gradients, $\nabla_{\mathbf{x}}\mathbf{n}_1$ and $\nabla_{\mathbf{x}}\mathbf{n}_2$, have been derived in [Tamstorf and Grinspun 2013]. To compute the dihedral angle Hessian $\mathbf{G}$, we also need $\nabla_{\mathbf{x}}h_1$, $\nabla_{\mathbf{x}}h_2$, $\nabla_{\mathbf{x}}\omega_1$ and $\nabla_{\mathbf{x}}\omega_2$ to compute $\nabla_{\mathbf{x}}\mathbf{t}_1$ and $\nabla_{\mathbf{x}}\mathbf{t}_2$. The derivation of these gradients has been presented in detail in Appendix A.

4.1.1 Matrix expression. For a dihedral element depicted in Fig. 2, let $\mathbf{e}$ be the normalized direction of the hinge edge, $\mathbf{m}_1$ and $\mathbf{m}_2$ be normalized altitude vectors. To understand the indefiniteness of the dihedral angle Hessian $\mathbf{G}$, we provide its compact matrix expression,

$$\begin{aligned} \mathbf{G} &= \mathbf{G}_m + \mathbf{G}_e, \\ \mathbf{G}_m &= (\mathbf{t}_1\mathbf{t}_1^\top) \otimes \mathbf{A}_1 + (\mathbf{t}_2\mathbf{t}_2^\top) \otimes \mathbf{A}_2 + \tfrac{1}{2}(\mathbf{s}\mathbf{s}^\top) \otimes (\mathbf{A}_1 + \mathbf{A}_2), \\ \mathbf{G}_e &= \mathbf{B}_1 + \mathbf{B}_1^\top + \mathbf{B}_2 + \mathbf{B}_2^\top, \end{aligned} \tag{4}$$

where $\mathbf{s} = l^{-1}[1, -1, 0, 0]^\top$, $\mathbf{A}_1 = \mathbf{m}_1\mathbf{n}_1^\top + \mathbf{n}_1\mathbf{m}_1^\top$ and $\mathbf{A}_2 = \mathbf{m}_2\mathbf{n}_2^\top + \mathbf{n}_2\mathbf{m}_2^\top$ are matrices in $\mathbb{R}^{3\times3}$, $\mathbf{B}_1 = (\mathbf{t}_1\mathbf{s}^\top) \otimes (\mathbf{e}\mathbf{n}_1^\top)$ and $\mathbf{B}_2 = (\mathbf{t}_2\mathbf{s}^\top) \otimes (\mathbf{e}\mathbf{n}_2^\top)$ are matrices in $\mathbb{R}^{12\times12}$. $\mathbf{G}$ is indefinite because of the presence of indefinite matrices $\mathbf{A}_1$, $\mathbf{A}_2$, $\mathbf{B}_1 + \mathbf{B}_1^\top$ and $\mathbf{B}_2 + \mathbf{B}_2^\top$ which have both positive and negative eigenvalues. For more details on our derivation, please refer to Appendix A. In spite of the indefiniteness of $\mathbf{G}$, we cannot assert with certainty that the energy Hessian $\mathbf{H}$ is indefinite due to the presence of $\mathbf{P}$. In Section. 4.2, our analytic eigensystem is the first to reveal that $\mathbf{H}$ typically has four positive and four negative eigenvalues, in addition to four known zero eigenvalues.

As opposed to using complex Hessian projection techniques, a simpler approach to eliminate the indefiniteness issue is to omit $\mathbf{G}$ and approximate the Hessian as $\mathbf{H} \approx \mu p \mathbf{P}$. However, this approach may not guarantee positive semi-definiteness for some models that could result in a negative p. On the other hand, the Gauss-Newton method also omits $\mathbf{G}$ but ensures the positive semi-definiteness for models with a quadratic energy $\psi(\theta, \bar{\theta}) = \frac{1}{2}c^2(\theta, \bar{\theta})$ by using the approximation $\mathbf{H} \approx \mu(\partial c/\partial\theta)^2\mathbf{P}$, except for *Bridson's model.*

4.1.2 Geometric stiffness. However, $\mathbf{G}$ serves as geometric stiffness that controls the direction of displacements caused by bending force and omitting it can result in instability in some cases. The importance of the geometric stiffness have been demonstrated by Tournier et al. [2015] for a mass-spring system to suppress oscillations, and Choi and Ko [2002] suggested omitting the negative definite geometric stiffness only when a spring is compressed. In Section. 4.2.1, we have described the twelve motion modes of a dihedral element in detail. We are interested in which displacement modes will be preserved under the effect of $\mathbf{H}$. When solving a displacement equation $\mathbf{H}\Delta\mathbf{x} = \mathbf{f}$ to find a Newton's direction, $\mathbf{P}$ only restricts the projection length of $\Delta\mathbf{x}$ on the bending force $\mathbf{f}$ and allows all the motion modes. To reveal the effect of geometric stiffness, we need to analyze the following two expressions,

$$\mathbf{G}_m\Delta\mathbf{x} = \mathbf{t}_1 \otimes (\mathbf{A}_1\mathbf{y}_1) + \mathbf{t}_2 \otimes (\mathbf{A}_2\mathbf{y}_2) + \frac{1}{2}\mathbf{s} \otimes (\mathbf{A}_1\mathbf{y}_3 + \mathbf{A}_2\mathbf{y}_3),$$

$$\mathbf{G}_e\Delta\mathbf{x} = (\mathbf{n}_1^\top\mathbf{y}_3)\mathbf{t}_1 \otimes \mathbf{e} + (\mathbf{n}_2^\top\mathbf{y}_3)\mathbf{t}_2 \otimes \mathbf{e} + (\mathbf{e}^\top\mathbf{y}_1)\mathbf{s} \otimes \mathbf{n}_1 + (\mathbf{e}^\top\mathbf{y}_2)\mathbf{s} \otimes \mathbf{n}_2,$$

where $\mathbf{y}_1 = \sum \mathbf{t}_1[i]\Delta\mathbf{x}_i$ and $\mathbf{y}_2 = \sum \mathbf{t}_2[i]\Delta\mathbf{x}_i$ are relative displacements on the two adjacent triangles, respectively, and $\mathbf{y}_3 = \sum \mathbf{s}[i]\Delta\mathbf{x}_i$ on the hinge edge. Because $\mathbf{e}$ is not contained in $\mathbf{f}$, it follows that $\mathbf{n}_1^\top\mathbf{y}_3 = 0$ and $\mathbf{n}_2^\top\mathbf{y}_3 = 0$, implying that $\mathbf{y}_3$ is parallel to $\mathbf{e}$. Consequently, we have $\mathbf{A}_1\mathbf{y}_3 + \mathbf{A}_2\mathbf{y}_3 = \mathbf{0}$ resulting in the disappearance of $\mathbf{s}$ in $\mathbf{G}_m\Delta\mathbf{x}$. Because $\mathbf{s}$ is independent on $\mathbf{t}_1$ and $\mathbf{t}_2$, $\mathbf{s} \otimes \mathbf{n}_1$ and $\mathbf{s} \otimes \mathbf{n}_2$ are not contained in $\mathbf{f}$, which also necessitates the elimination of $\mathbf{s}$ in $\mathbf{G}_e\Delta\mathbf{x}$, leading to $\mathbf{e}^\top\mathbf{y}_1 = 0$ and $\mathbf{e}^\top\mathbf{y}_2 = 0$. In addition, $\mathbf{A}_1\mathbf{y}_1$ should not contain $\mathbf{m}_1$ and $\mathbf{A}_2\mathbf{y}_2$ should not contain $\mathbf{m}_2$. Therefore, we conclude that $\mathbf{y}_1$ is parallel to $\mathbf{m}_1$ and $\mathbf{y}_2$ is parallel to $\mathbf{m}_2$. Putting aside zero-eigenvalue motion modes, the remaining motion modes for a dihedral element under the effect of $\mathbf{H}$ are altitude changes, i.e. $\Delta\mathbf{x} = -[\mathbf{0}^\top, \mathbf{0}^\top, h_1\mathbf{m}_1^\top, h_2\mathbf{m}_2^\top]^\top$, as depicted in Fig. 4(b). This implies that the indefinite energy Hessian $\mathbf{H}$ tends to over-stretch the

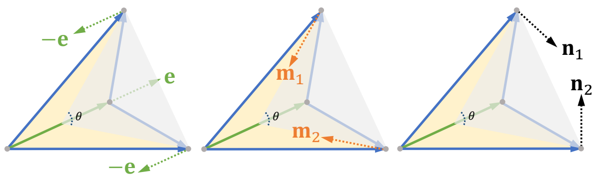

(a) Barycentric sliding (b) Altitude changing (c) Bending

Fig. 4. Nonzero-eigenvalue modes. (a) Barycentric sliding corresponds to displacements of $\boldsymbol{\nu}_4$ and $\boldsymbol{\nu}_5$ defined in Eq. 5. (b) Altitude changing corresponds to displacements of $\boldsymbol{\nu}_6$ and $\boldsymbol{\nu}_7$. (c) Bending correspond to displacements of $\boldsymbol{\nu}_8$ and $\boldsymbol{\nu}_9$.

dihedral element along the altitude directions. When using only one Newton's iteration without a line search, no mechanism is in place to mitigate this detrimental consequence. As illustrated by Fig. 5(a), the right side of the cylinder shell undesirably expands during the twisting process. In scenarios involving low BMR and small bending deformation, a sufficiently strong membrane stiffness can alleviate the negative impact of an inappropriate geometric stiffness of DAB models. However, this negative effect can be more pronounced in the cases of high BMR and large bending deformation, where the geometric stiffness plays a dominant role. As illustrated in Fig. 7(g), Fig. 8 and Fig. 10(a, b), the Gauss-Newton approximation, lacking geometric stiffness, exhibits instability with oscillations. Additionally, as shown in Fig. 7(e, f), Hessian projections incorporating inappropriate geometric stiffness fail to stably simulate the compressing cylinder.

4.2 Analytic Eigensystem

We note that performing a full eigenanalysis of DAB models can provide a complete understanding of the nature of the energy Hessian and its eigenvalues. This information is crucial for determining the positive semi-definiteness or indefiniteness of $\mathbf{H}$ and addressing the indefiniteness issue. While previous works, such as [Bridson et al. 2003] and [Tamstorf and Grinspun 2013], have described the twelve distinct motion modes of a dihedral element and identified four zero eigenvalues, a full eigenanalysis has not been conducted until this work. By performing this analysis, we can gain insight into the behaviors of the model and potentially improve its performance.

4.2.1 The twelve modes. At the beginning of our eigenanalysis, we were faced with uncertainty. Fortunately, the twelve motion modes described by [Bridson et al. 2003] provide us a valuable guidance. These modes consists of three translations and three rotations representing rigid body motions, as well as two in-plane displacements for vertex $\mathbf{x}_2$ and vertex $\mathbf{x}_3$, the in-line stretching of the hinge edge, and a bending mode. To aid in our eigenanalysis for DAB models, we construct twelve displacement vectors that represent each of these motion modes explicitly.

Zero-eigenvalue modes. Constructing four zero-eigenvalue eigenvectors, namely $\boldsymbol{\nu}_0$, $\boldsymbol{\nu}_1$, $\boldsymbol{\nu}_2$, and $\boldsymbol{\nu}_3$ in Eq. 5, it is easy to verify that all of them satisfy $\mathbf{H}\boldsymbol{\nu}_i = \mathbf{0}$, and they correspond to three rigid translations and the uniform scaling along the hinge edge, respectively.

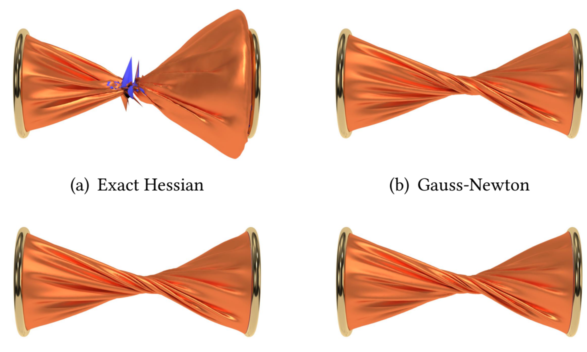

(a) Exact Hessian (b) Gauss-Newton

(c) **H**-projection (d) **F**-projection

Fig. 5. A twisting cylinder example. The simulation fails if using the exact indefinite energy Hessian. The other three methods all produce positive semi-definite Hessian and can stably simulate the twisting cylinder.

Nonzero-eigenvalue modes. For nonzero eigenvalues, there are eight motion modes or their combinations. As depicted in Fig. 4(a), barycentric sliding motions along the hinge edge of vertex $\mathbf{x}_2$ and $\mathbf{x}_3$ can be defined as $\boldsymbol{\nu}_4$ and $\boldsymbol{\nu}_5$, respectively. They do not affect the bending energy but alter the distribution of bending forces on the hinge edge. Similarly, we can define $\boldsymbol{\nu}_6$ and $\boldsymbol{\nu}_7$ for altitude-changing motions of vertex $\mathbf{x}_2$ and $\mathbf{x}_3$, respectively, , as depicted in Fig. 4(b). They do not affect the bending energy but change the magnitude of bending forces. The bending modes correspond to dihedral angle changes without introducing in-plane deformation and rigid transformation, which can be represented by rotating vertex $\mathbf{x}_2$ and $\mathbf{x}_3$ around the hinge edge respectively. Therefore, we can define $\boldsymbol{\nu}_8$ and $\boldsymbol{\nu}_9$ for instance bending displacements of vertex $\mathbf{x}_2$ and $\mathbf{x}_3$, respectively, as depicted in Fig. 4(c). The only remaining modes are the three rigid rotations. The rotation around $\mathbf{e}$ is linearly relative to the two bending modes. Therefore, only rotations around $\mathbf{n}_1$ and $\mathbf{m}_1$ need to be considered. The displacements of vertex $\mathbf{x}_2$ and $\mathbf{x}_3$ can be ignored because they are linearly relative to the sliding motions and altitude changes when rigid rotations occur. Assuming the midpoint of the hinge edge is the rotation origin, we can define $\boldsymbol{\nu}_{10}$ and $\boldsymbol{\nu}_{11}$ for rotation around $\mathbf{m}_1$ and $\mathbf{n}_1$, respectively.

$$
\begin{aligned}
\boldsymbol{\nu}_0 &= [1,1,1,1]^\top \otimes \mathbf{n}_1, & \boldsymbol{\nu}_1 &= [1,1,1,1]^\top \otimes \mathbf{m}_1,\\
\boldsymbol{\nu}_2 &= [1,1,1,1]^\top \otimes \mathbf{e}, & \boldsymbol{\nu}_3 &= [0,1,\omega_1,\omega_2]^\top \otimes \mathbf{e},\\
\boldsymbol{\nu}_4 &= [0,0,1,0]^\top \otimes \mathbf{e}, & \boldsymbol{\nu}_5 &= [0,0,0,1]^\top \otimes \mathbf{e},\\
\boldsymbol{\nu}_6 &= [0,0,1,0]^\top \otimes \mathbf{m}_1, & \boldsymbol{\nu}_7 &= [0,0,0,1]^\top \otimes \mathbf{m}_2,\\
\boldsymbol{\nu}_8 &= [0,0,1,0]^\top \otimes \mathbf{n}_1, & \boldsymbol{\nu}_9 &= [0,0,0,1]^\top \otimes \mathbf{n}_2,\\
\boldsymbol{\nu}_{10} &= [1,-1,0,0]^\top \otimes \mathbf{n}_1, & \boldsymbol{\nu}_{11} &= [1,-1,0,0]^\top \otimes \mathbf{m}_1.
\end{aligned}
\tag{5}
$$

Although the eight vectors $\boldsymbol{\nu}_j (j \in \{4, ..., 11\})$ are orthogonal to each other, they are not eigenvectors of $\mathbf{H}$ because they do not satisfy $\mathbf{H}\boldsymbol{\nu}_j = \lambda_j \boldsymbol{\nu}_j$ and are not orthogonal to the zero-eigenvalue eigenvectors $\boldsymbol{\nu}_i (i \in \{0, ..., 3\})$. However, the expressions of $\mathbf{H}\boldsymbol{\nu}_j$ (presented in detail in Appendix. B.1) guide us to find an invariant subspace of $\mathbf{H}$, based on which we can discover an intrinsic decomposition of $\mathbf{H}$.

4.2.2 Intrinsic decomposition. Directly analyzing the eigensystem of the energy Hessian $\mathbf{H}$ is a challenging task. However, inspired by the methods of [Smith et al. 2019; Teran et al. 2005], which cannot be

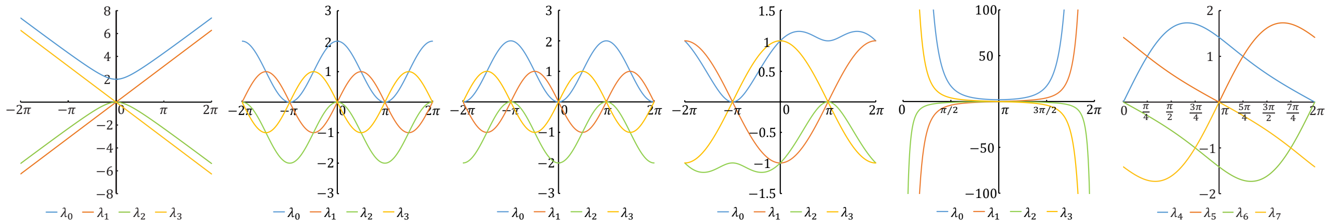

(a) *Discrete Shells*: $\Delta\theta$ (b) *Cubic Shells*: $\Delta\theta$ (c) *DWE*: θ (d) *Bridson's model*: θ (e) *Tamstorf's model*: θ (f) Eigenvalues of $\mathbf{F}_1/g$: θ

Fig. 6. (a-e) are depicts of eigenvalues of $\mathbf{F}_0$ for different DAB models with different x-axis. (a) *Discrete Shells* has $g = \Delta\theta$ and $p = 1$, with the x-axis as $\Delta\theta \in (-2\pi, 2\pi)$. (b) *Cubic Shells* has $g=\sin(\Delta\theta)$ and $p=\cos(\Delta\theta)$, with the x-axis as $\Delta\theta \in (-2\pi, 2\pi)$. (c) *Discrete Willmore Energy* (DWE) has $g=-\sin\theta$ and $p=-\cos\theta$, with the x-axis as $\theta \in (-2\pi, 2\pi)$. (d) *Bridson's model* has $g=-\cos\frac{\theta}{2}+\cos\frac{\bar\theta}{2}$ and $p=\frac{1}{2}\sin\frac{\theta}{2}$, with $\bar\theta=\pi$ and the x-axis as $\theta\in(-2\pi,2\pi)$. (e) *Tamstorf's model* has $g=2\sin\frac{\Delta\theta}{2}/\left(\sin^3\frac{\theta}{2}\sin\frac{\bar\theta}{2}\right)$ and $p=\left(\cos\frac{\Delta\theta}{2}-3\sin\frac{\Delta\theta}{2}\cot\frac{\theta}{2}\right)/\left(\sin^3\frac{\theta}{2}\sin\frac{\bar\theta}{2}\right)$, with $\bar\theta=\pi$ and the x-axis as $\theta\in(0,2\pi)$. (f) is the depict of eigenvalues of $\mathbf{F}_1/g$ for all these models, with $g\neq 0$ and the x-axis as $\theta\in(0,2\pi)$.

applied to DAB models, we aim to find an intrinsic decomposition of $\mathbf{H}$ to obtain an intrinsic bending matrix whose analytic eigensystem is possible. The construction of the intrinsic decomposition is due to an important discovery from the twelve motion modes: there are eight linearly independent vectors $\mathbf{Z}=\left[\boldsymbol{\zeta}_0,\ldots,\boldsymbol{\zeta}_7\right]\in\mathbb{R}^{12\times 8}$ that appear repeatedly in the expressions of $\mathbf{H}\boldsymbol{\nu}_j$, which are

$$\begin{array}{llll}\boldsymbol{\zeta}_0=\mathbf{t}_1\otimes\mathbf{n}_1, & \boldsymbol{\zeta}_1=\mathbf{t}_2\otimes\mathbf{n}_1, & \boldsymbol{\zeta}_2=\mathbf{t}_2\otimes\mathbf{m}_1, & \boldsymbol{\zeta}_3=\mathbf{t}_1\otimes\mathbf{m}_1\\ \boldsymbol{\zeta}_4=\mathbf{s}\otimes\mathbf{n}_1, & \boldsymbol{\zeta}_5=\mathbf{s}\otimes\mathbf{m}_1, & \boldsymbol{\zeta}_6=\mathbf{t}_2\otimes\mathbf{e}, & \boldsymbol{\zeta}_7=\mathbf{t}_1\otimes\mathbf{e}.\end{array} \tag{6}$$

The reason $\mathbf{n}_2$ and $\mathbf{m}_2$ are not included in $\mathbf{Z}$ is that they are linearly dependent on $\mathbf{n}_1$ and $\mathbf{m}_1$. Please refer to Appendix. B.1 for more details on the discovery of $\mathbf{Z}$. The column space of $\mathbf{Z}$ is an invariant subspace of $\mathbf{H}$ because of $\mathbf{HZ}=\mu\mathbf{ZFZ}^\mathsf{T}\mathbf{Z}$, where $\mathbf{F}\in\mathbb{R}^{8\times 8}$ is only related to intrinsic bending deformation of a dihedral element. The detailed derivation of $\mathbf{F}$ can be found in Appendix. B.2. Because $\mathbf{Z}$ has a full column rank, we obtain an important decomposition of the energy Hessian of DAB models, i.e.

$$\mathbf{H}=\mu\mathbf{ZFZ}^\mathsf{T}. \tag{7}$$

Interestingly, $\mathbf{F}$ is a block-diagonal matrix thanks to the order of $\boldsymbol{\zeta}$s in $\mathbf{Z}$. Specifically, the upper-left block is

$$\mathbf{F}_0=\begin{bmatrix} p & -p\cos\theta & p\sin\theta & g\\ -p\cos\theta & p\cos^2\theta-g\sin 2\theta & -\frac{p}{2}\sin 2\theta-g\cos 2\theta & 0\\ p\sin\theta & -\frac{p}{2}\sin 2\theta-g\cos 2\theta & p\sin^2\theta+g\sin 2\theta & 0\\ g & 0 & 0 & 0\end{bmatrix},$$

and the bottom-right block is

$$\mathbf{F}_1=g\begin{bmatrix} -\sin\theta\cos\theta & \sin^2\theta & -\cos\theta & 1\\ \sin^2\theta & \sin\theta\cos\theta & \sin\theta & 0\\ -\cos\theta & \sin\theta & 0 & 0\\ 1 & 0 & 0 & 0\end{bmatrix}.$$

Notably, $\mathbf{F}$ depends only on dihedral angles because g and p are only dependent on θ and $\bar\theta$.

4.2.3 Analytic eigenvalues and eigenvectors. By exploiting the symbolic calculation capabilities of Mathematica to solve the characteristic polynomials of $\mathbf{F}_0$ and $\mathbf{F}_1$, we successfully obtain the analytic eigenvalues of $\mathbf{F}$, i.e.

$$\begin{array}{ll}\lambda_0=p+\sqrt{p^2+g^2}, & \lambda_4=\frac{g}{2}\left(\sin\theta+\sqrt{\sin^2\theta+4(1-\cos\theta)}\right),\\ \lambda_1=g, & \lambda_5=\frac{g}{2}\left(-\sin\theta+\sqrt{\sin^2\theta+4(1+\cos\theta)}\right),\\ \lambda_2=p-\sqrt{p^2+g^2}, & \lambda_6=\frac{g}{2}\left(\sin\theta-\sqrt{\sin^2\theta+4(1-\cos\theta)}\right),\\ \lambda_3=-g, & \lambda_7=\frac{g}{2}\left(-\sin\theta-\sqrt{\sin^2\theta+4(1+\cos\theta)}\right),\end{array} \tag{8}$$

in which $\{\lambda_0,\lambda_1,\lambda_2,\lambda_3\}$ and $\{\lambda_4,\lambda_5,\lambda_6,\lambda_7\}$ are eigenvalues of $\mathbf{F}_0$ and $\mathbf{F}_1$, respectively. The eigenvalues of $\mathbf{F}_0$ for different models have been depicted in Fig. 6(a-e). Only *Tamstorf's model* has unbounded $\mathbf{F}_0$ eigenvalues due to its unbounded bending energy. The eigenvalues of $\mathbf{F}_1/g$ ($g\neq 0$) depicted in Fig. 6(f) are the same for all these models, which reveals that additional zero eigenvalues appear at $\theta=0,\pi,2\pi$.

If a dihedral element has no bending deformation with $g=0$, $\mathbf{F}$ has only one nonzero eigenvalue $\lambda=2p$. The corresponding eigenvector is $\boldsymbol{\epsilon}=\frac{1}{\sqrt{2}}\left[1,-\cos\theta,\sin\theta,0,0,0,0,0,\right]^\mathsf{T}$ and $\mathbf{Z}\boldsymbol{\epsilon}$ is the eigenvector of $\mathbf{H}$ because of $\mathbf{P}=\lambda\mathbf{Z}\boldsymbol{\epsilon}\left(\mathbf{Z}\boldsymbol{\epsilon}\right)^\mathsf{T}$. Otherwise in the case of $g>0$ ($g<0$), $\mathbf{F}$ has four positive eigenvalues $\{\lambda_0,\lambda_1(\lambda_3),\lambda_4(\lambda_6),\lambda_5(\lambda_7)\}$ and four negative eigenvalues $\{\lambda_2,\lambda_3(\lambda_1),\lambda_6(\lambda_4),\lambda_7(\lambda_5)\}$. The corresponding eigenvectors of $\mathbf{F}_0$ are

$$\hat{\boldsymbol{\epsilon}}_0=\hat{\boldsymbol{\epsilon}}(\lambda_0,1),\quad \hat{\boldsymbol{\epsilon}}_1=\hat{\boldsymbol{\epsilon}}(\lambda_1,-1),\quad \hat{\boldsymbol{\epsilon}}_2=\hat{\boldsymbol{\epsilon}}(\lambda_2,1),\quad \hat{\boldsymbol{\epsilon}}_3=\hat{\boldsymbol{\epsilon}}(\lambda_3,-1),$$

and eigenvectors of $\mathbf{F}_1$ are

$$\tilde{\boldsymbol{\epsilon}}_4=\tilde{\boldsymbol{\epsilon}}(\lambda_4,1),\quad \tilde{\boldsymbol{\epsilon}}_5=\tilde{\boldsymbol{\epsilon}}(\lambda_5,-1),\quad \tilde{\boldsymbol{\epsilon}}_6=\tilde{\boldsymbol{\epsilon}}(\lambda_6,1),\quad \tilde{\boldsymbol{\epsilon}}_7=\tilde{\boldsymbol{\epsilon}}(\lambda_7,-1),$$

in which

$$\begin{aligned}\hat{\boldsymbol{\epsilon}}(\lambda,\delta)&=\left[\frac{\lambda}{g},\delta\left(\sin\theta-\cos\theta\frac{\lambda}{g}\right),\delta\left(\cos\theta+\sin\theta\frac{\lambda}{g}\right),1\right]^\mathsf{T},\\ \tilde{\boldsymbol{\epsilon}}(\lambda,\delta)&=\left[\frac{\lambda}{g},\frac{\lambda}{g}\frac{\sin\theta}{\delta-\cos\theta},\delta,1\right]^\mathsf{T},\end{aligned} \tag{9}$$

with $\delta=\pm1$ as a sign indicator, are the general expressions of eigenvectors of $\mathbf{F}_0$ and $\mathbf{F}_1$, respectively. One thing to note is that $\tilde{\boldsymbol{\epsilon}}(\lambda,\delta)$ is not continuous in some special cases where $\mathbf{F}_1$ has zero eigenvalues:

- If $\theta=0$ or $\theta=2\pi$, there are $\lambda_4=0$ and $\lambda_6=0$. As a result, we can choose $\tilde{\boldsymbol{\epsilon}}_4=[0,1+\sqrt{3},1,1]^\mathsf{T}$ and $\tilde{\boldsymbol{\epsilon}}_6=[0,1-\sqrt{3},1,1]^\mathsf{T}$;
- If $\theta=\pi$, there are $\lambda_5=0$ and $\lambda_7=0$. As a result, we can choose $\tilde{\boldsymbol{\epsilon}}_5=[0,1+\sqrt{3},-1,1]^\mathsf{T}$ and $\tilde{\boldsymbol{\epsilon}}_7=[0,1-\sqrt{3},-1,1]^\mathsf{T}$. Note: $1+\sqrt{3}$ and $1-\sqrt{3}$ are the left and right limits of $\frac{\lambda}{g}\frac{\sin\theta}{\delta-\cos\theta}$, respectively.

Consequently, we obtain the analytic eigendecomposition of the intrinsic bending matrix, i.e.

$$\mathbf{F} = \mathbf{E}\mathbf{\Lambda}\mathbf{E}^{\mathsf{T}}, \tag{10}$$

in which $\mathbf{E} \in \mathbb{R}^{8\times 8}$ is an orthogonal matrix with columns as the normalized eigenvectors of $\mathbf{F}$, and $\mathbf{\Lambda} = diag\{\lambda_0, \ldots, \lambda_7\} \in \mathbb{R}^{8\times 8}$ is a diagonal matrix. Combing Eq. 7 and Eq. 10 yields a new decomposition of the energy Hessian, i.e. $\mathbf{H} = \mu(\mathbf{ZE})\mathbf{\Lambda}(\mathbf{ZE})^{\mathsf{T}}$. However, because of the non-orthogonality of matrix $\mathbf{ZE}$, the eigenvalues of $\mathbf{F}$ are not the eigenvalues of $\mathbf{H}$. Nonetheless, we prove based on Sylvester's law of inertia that the numbers of positive, negative, and zero eigenvalues of $\mathbf{H}$ are the same as those of $\mathbf{F}$, which means that $\mathbf{H}$ also typically has four positive eigenvalues and four negative eigenvalues, as well as four zero eigenvalues. For more information on our proof, please refer to Appendix. B.2.

4.2.4 **F**-*projection.* Although the intrinsic decomposition in Eq. 7 is not a similarity transform and can modify the spectrum, the positive semi-definiteness of $\mathbf{F}$ guarantees the positive-semi definiteness of $\mathbf{H}$. In order to restore the positive semi-definiteness of $\mathbf{H}$, we can perform direct modifications of $\mathbf{H}$, referred to as $\mathbf{H}$-projection, or direct modifications of $\mathbf{F}$, referred to as $\mathbf{F}$-projection. However, as far as we know, the $\mathbf{H}$-projection can only be performed numerically using the SVD. Using the analytic eigensystem of $\mathbf{F}$ in Eq. 10, we can restore the positive semi-definiteness of $\mathbf{H}$ by setting negative eigenvalues of $\mathbf{F}$ to zero or a small positive value, such as $1e^{-6}$. We have summarized our $\mathbf{F}$-projection algorithm for DAB models in Algorithm. 1, which is more than 30 times faster than the SVD-based $\mathbf{H}$-projection implemented using the *eigenvalue()* and *eigenvectors()* interfaces from *Eigen* library on the CPU.

As illustrated by the examples of twisting in Fig. 5 and the compressing example in Fig. 17, our $\mathbf{F}$-projection produces stable simulations. However, the $\mathbf{F}$-projection fails to stabilize the simulation of a cylinder plate with a high bending-membrane ratio in the compressing example in Fig. 7. To understand this failure, we consider the $\mathbf{F}$-projected Hessian with $g > 0$, which is the sum of four positive semi-definite projection matrices, denoted by

$$\mathbf{H}' = \mu(\lambda_0\mathbf{v}_0\mathbf{v}_0^{\mathsf{T}} + \lambda_1\mathbf{v}_1\mathbf{v}_1^{\mathsf{T}} + \lambda_4\mathbf{v}_4\mathbf{v}_4^{\mathsf{T}} + \lambda_5\mathbf{v}_5\mathbf{v}_5^{\mathsf{T}}), \tag{11}$$

where $\mathbf{v}_i = \mathbf{Z}\boldsymbol{\epsilon}_i$ corresponding to positive eigenvalues of $\mathbf{F}$ are

$$\mathbf{v}_0 = \frac{1}{\|\hat{\boldsymbol{\epsilon}}_0\|}\left(\frac{\lambda_0}{g}\mathbf{q}_0 + \mathbf{q}_2\right), \qquad \mathbf{v}_1 = \frac{1}{\|\hat{\boldsymbol{\epsilon}}_1\|}\left(\frac{\lambda_1}{g}\mathbf{q}_1 + \mathbf{q}_3\right),$$
$$\mathbf{v}_4 = \frac{1}{\|\hat{\boldsymbol{\epsilon}}_4\|}\left(\frac{\lambda_4\mathbf{q}_6}{g(1-\cos\theta)} + \mathbf{q}_4\right), \qquad \mathbf{v}_5 = \frac{1}{\|\hat{\boldsymbol{\epsilon}}_5\|}\left(\frac{\lambda_5\mathbf{q}_7}{g(1+\cos\theta)} + \mathbf{q}_5\right),$$

which are the combination of eight independent vectors in $\mathbb{R}^{12}$,

$$\begin{aligned} \mathbf{q}_0 &= \mathbf{t}_1 \otimes \mathbf{n}_1 + \mathbf{t}_2 \otimes \mathbf{n}_2, & \mathbf{q}_1 &= \mathbf{t}_1 \otimes \mathbf{n}_1 - \mathbf{t}_2 \otimes \mathbf{n}_2, \\ \mathbf{q}_2 &= \mathbf{t}_1 \otimes \mathbf{m}_1 + \mathbf{t}_2 \otimes \mathbf{m}_2, & \mathbf{q}_3 &= \mathbf{t}_1 \otimes \mathbf{m}_1 - \mathbf{t}_2 \otimes \mathbf{m}_2, \\ \mathbf{q}_4 &= \mathbf{t}_1 \otimes \mathbf{e} + \mathbf{t}_2 \otimes \mathbf{e}, & \mathbf{q}_5 &= \mathbf{t}_1 \otimes \mathbf{e} - \mathbf{t}_2 \otimes \mathbf{e}, \\ \mathbf{q}_6 &= \mathbf{s} \otimes \mathbf{n}_1 + \mathbf{s} \otimes \mathbf{n}_2, & \mathbf{q}_7 &= \mathbf{s} \otimes \mathbf{n}_1 - \mathbf{s} \otimes \mathbf{n}_2. \end{aligned} \tag{12}$$

Similarly, we also analyze $\mathbf{H}'$ by solving the displacement equation $\mathbf{H}'\Delta\mathbf{x}=\mathbf{f}$, in which the bending force $\mathbf{f}$ is parallel to $\mathbf{q}_0$. Because $\mathbf{m}_1$ and $\mathbf{e}$ are orthogonal to $\mathbf{n}_1$, $\mathbf{v}_0^{\mathsf{T}}\Delta\mathbf{x}$, $\mathbf{v}_1^{\mathsf{T}}\Delta\mathbf{x}$, $\mathbf{v}_4^{\mathsf{T}}\Delta\mathbf{x}$ and $\mathbf{v}_5^{\mathsf{T}}\Delta\mathbf{x}$ must be zero to eliminate $\mathbf{q}_2$, $\mathbf{q}_3$, $\mathbf{q}_4$ and $\mathbf{q}_5$ in $\mathbf{H}'\Delta\mathbf{x}$. The strong coupling between $\mathbf{q}_0$ and $\mathbf{q}_2$ in $\mathbf{v}_0$, among others, eliminate the solution space of this equation, indicating that all the twelve motion modes are excluded. As a result, it is difficult to obtain desirable displacements in the case of high BMR where bending force and Hessian dominate. This is supported by the low convergence of $\mathbf{F}$-projection in Fig. 12. Although we cannot explicitly analyze the $\mathbf{H}$-projection, its low convergence suggests that it also excludes all the motion modes.

ALGORITHM 1: F-based Hessian Projection

Input: Positions of a dihedral element: $\{\mathbf{x}_0, \mathbf{x}_1, \mathbf{x}_2, \mathbf{x}_3\}$
Output: The F-based projected Hessian: $\mathbf{H}'$

Compute $\theta, l, \omega_1, \omega_2, h_1, h_2, p, g$;
$\mathbf{t}_1 = h_1^{-1}[\omega_1 - 1, -\omega_1, 1, 0]$;
$\mathbf{t}_2 = h_2^{-1}[\omega_2 - 1, -\omega_2, 0, 1]$;
$\mathbf{s} = l^{-1}[1, -1, 0, 0]$;
Compute $\mathbf{n}_1, \mathbf{m}_1, \mathbf{e}$;
Compute eigenvalues $\mathbf{\Lambda}$; ▷ According to Eq. 8
Compute eigenvectors $\mathbf{E}$; ▷ According to Eq. 9
$\mathbf{\Lambda}' = Clamp(\mathbf{\Lambda})$; ▷ Clamp negative eigenvalues to zero
$\mathbf{F}' = \mathbf{E}\mathbf{\Lambda}'\mathbf{E}$; ▷ According to Eq. 10
$\mathbf{H}' = \mu\mathbf{Z}\mathbf{F}'\mathbf{Z}^{\mathsf{T}}$. ▷ According to Eq. 11

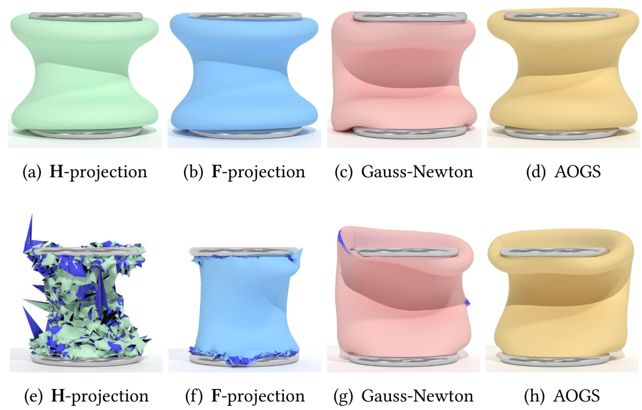

Fig. 7. This is a virtual cylinder plate with a high BMR. When it is compressed by the top ring, all the four methods can stably simulate the cylinder at the beginning, as shown by figures (a-e). As the top ring goes down to figures (e-h), H-projection, our F-projection and the Gauss-Newton approximation all fail. After applying our orthotropic geometric stiffness, the cylinder can be stably compressed to the bottom.

4.3 Adaptive Orthotropic Geometric Stiffness (AOGS)

The exact geometric stiffness matrix $\mathbf{G}$ is indefinite and retains only the altitude-changing modes, which are undesirable for dihedral elements. While $\mathbf{H}$-projection and $\mathbf{F}$-projection are positive semi-definite, their geometric stiffness eliminate all motion modes and result in unstable simulations. On the other hand, the Gauss-Newton method is positive semi-definite but permits all motion modes, which is too permissive. The Levenberg-Marquardt algorithm (LMA) adds a damping Hessian into the Gauss-Newton method, but it only damps the bending modes and has no effect on other modes. Besides zero-eigenvalue modes, the ideal geometric stiffness for DAB models must be positive semi-definite and should only keep the bending modes and eliminate other non-bending modes.

4.3.1 Directional Geometric Stiffness. We notice that there exist undesirable couplings in our **F**-projection Hessian $\mathbf{H}'$ between some $\mathbf{q}_i/\mathbf{q}_j$ pairs, such as $\mathbf{q}_0/\mathbf{q}_2$, $\mathbf{q}_1/\mathbf{q}_3$, $\mathbf{q}_4/\mathbf{q}_6$, and $\mathbf{q}_5/\mathbf{q}_7$. This motivates us to conjecture that the bending modes can be released by removing these couplings. Therefore, the resulting Hessian is

$$\mathbf{H}_d = \mu \sum_{i=0}^{7} \alpha_i \mathbf{q}_i \mathbf{q}_i^\top, \quad \alpha_i > 0,$$

which is a combination of stiffness matrix $\mathbf{P} = \mathbf{q}_0\mathbf{q}_0^\top$ and seven directional geometric stiffness terms $\mathbf{q}_i\mathbf{q}_i^\top$. To verify the effectiveness of these directions, we need to analyze the solution of the displacement equation $\mathbf{H}_d\Delta\mathbf{x} = \mathbf{f}$. Because only $\mathbf{q}_0$ is parallel to the bending force $\mathbf{f}$, displacements along other directions should be eliminated (or damped), implying $(\mathbf{q}_i\mathbf{q}_i^\top)\Delta\mathbf{x} = \mathbf{0}$ for $i \neq 0$. Considering $\mathbf{q}_2^\top\Delta\mathbf{x} = 0$ and $\mathbf{q}_4^\top\Delta\mathbf{x} = 0$, we obtain two constraints for the target displacement,

$$\mathbf{m}_1^\top\mathbf{y}_1 + \mathbf{m}_2^\top\mathbf{y}_2 = 0, \quad \textit{and} \quad \mathbf{e}^\top\mathbf{y}_1 + \mathbf{e}^\top\mathbf{y}_2 = 0,$$

in which $\mathbf{y}_{1,2}$ are relative displacements (Table. 1). Considering $\mathbf{q}_1^\top\Delta\mathbf{x}=0$, $\mathbf{q}_3^\top\Delta\mathbf{x}=0$ and $\mathbf{q}_5^\top\Delta\mathbf{x}=0$, we obtain three constraints,

$$\mathbf{n}_1^\top\mathbf{y}_1 - \mathbf{n}_2^\top\mathbf{y}_2 = 0,\ \mathbf{m}_1^\top\mathbf{y}_1 - \mathbf{m}_2^\top\mathbf{y}_2 = 0,\ \textit{and}\ \mathbf{e}^\top\mathbf{y}_1 - \mathbf{e}^\top\mathbf{y}_2 = 0.$$

By combining all the five constraints, we conclude that $\mathbf{y}_1$ is parallel to $\mathbf{n}_1$, $\mathbf{y}_2$ is parallel to $\mathbf{n}_2$ and $\|\mathbf{y}_1\| = \|\mathbf{y}_2\|$. Excluding rigid translations, we obtain the expression of the target displacement,

$$\Delta\mathbf{x} = -\frac{1}{\alpha_0}\left([\mathbf{0}^\top, \mathbf{0}^\top, h_1\mathbf{n}_1^\top, h_2\mathbf{n}_2^\top]^\top + [0, 1, \omega_1, \omega_2]^\top \otimes \mathbf{y}_3\right),$$

including the bending modes and uniform scaling along arbitrary directions. To further eliminate undesirable (uniform) scaling orthogonal to $\mathbf{e}$, we consider $\mathbf{q}_6^\top\Delta\mathbf{x}=0$ and $\mathbf{q}_7^\top\Delta\mathbf{x}=0$ to get another two constraints,

$$\mathbf{n}_1^\top\mathbf{y}_3 + \mathbf{n}_2^\top\mathbf{y}_3 = 0, \quad \textit{and} \quad \mathbf{n}_1^\top\mathbf{y}_3 - \mathbf{n}_2^\top\mathbf{y}_3 = 0,$$

for relative displacement on the hinge edge $\mathbf{y}_3$ being parallel to $\mathbf{e}$. The final displacement with zero-eigenvalue motion modes excluded is $\Delta\mathbf{x} = -\frac{1}{\alpha_0}[\mathbf{0}^\top, \mathbf{0}^\top, h_1\mathbf{n}_1^\top, h_2\mathbf{n}_2^\top]^\top$, as depicted in Fig. 4(c). These results demonstrate that the chosen directional geometric stiffness matrices retain only the bending modes of a dihedral element and eliminates other non-bending modes.

4.3.2 Orthotropic Geometric Stiffness. However, the difference between $\mathbf{q}_2$ and $\mathbf{q}_3$, for example, indicates that they are not reflection symmetric. If $\mathbf{q}_2\mathbf{q}_2^\top$ and $\mathbf{q}_3\mathbf{q}_3^\top$ are not imposed equally, coupling between $\mathbf{t}_1 \otimes \mathbf{m}_1$ and $\mathbf{t}_2 \otimes \mathbf{m}_2$ exists. To ensure reflection symmetry, some geometric stiffness pairs, such as $\mathbf{q}_2/\mathbf{q}_3$, $\mathbf{q}_4/\mathbf{q}_5$, and $\mathbf{q}_6/\mathbf{q}_7$, should be applied equally, except for $\mathbf{q}_0/\mathbf{q}_1$ due to the presence of $\mathbf{P}$ in $\mathbf{H}$. Consequently, we define four reflection-symmetric geometric stiffness matrices, specifically,

$$\begin{aligned}
\mathrm{S}_0 &= (\mathbf{q}_0\mathbf{q}_0^\top + \mathbf{q}_1\mathbf{q}_1^\top)/2 = (\mathbf{t}_1\mathbf{t}_1^\top)\otimes(\mathbf{n}_1\mathbf{n}_1^\top)+(\mathbf{t}_2\mathbf{t}_2^\top)\otimes(\mathbf{n}_2\mathbf{n}_2^\top),\\
\mathrm{S}_1 &= (\mathbf{q}_2\mathbf{q}_2^\top + \mathbf{q}_3\mathbf{q}_3^\top)/2 = (\mathbf{t}_1\mathbf{t}_1^\top)\otimes(\mathbf{m}_1\mathbf{m}_1^\top)+(\mathbf{t}_2\mathbf{t}_2^\top)\otimes(\mathbf{m}_2\mathbf{m}_2^\top),\\
\mathrm{S}_2 &= (\mathbf{q}_4\mathbf{q}_4^\top + \mathbf{q}_5\mathbf{q}_5^\top)/2 = (\mathbf{t}_1\mathbf{t}_1^\top+\mathbf{t}_2\mathbf{t}_2^\top)\otimes(\mathbf{e}\mathbf{e}^\top),\\
\mathrm{S}_3 &= (\mathbf{q}_6\mathbf{q}_6^\top + \mathbf{q}_7\mathbf{q}_7^\top)/2 = (\mathbf{s}\mathbf{s}^\top)\otimes(\mathbf{n}_1\mathbf{n}_1^\top+\mathbf{n}_2\mathbf{n}_2^\top).
\end{aligned} \tag{13}$$

The resulting Hessian is

$$\mathbf{H}_o = \mu\left[p\mathbf{P} + \alpha_0\mathrm{S}_0 + \alpha_1\mathrm{S}_1 + \alpha_2\mathrm{S}_2 + \alpha_3\mathrm{S}_3\right], \tag{14}$$

ALGORITHM 2: Adaptive Orthotropic Geometric Stiffness

Input: Positions of a dihedral element: $\{\mathbf{x}_0, \mathbf{x}_1, \mathbf{x}_2, \mathbf{x}_3\}$
Output: Hessian with adaptive orthotropic geometric stiffness: $\mathbf{H}_o$
1 Compute projected $\mathbf{F}'$; ▷ According to Algorithm. 1
2 Compute geometric stiffness: $\mathrm{S}_0, \mathrm{S}_1, \mathrm{S}_2, \mathrm{S}_3$; ▷ According to Eq. 13
3 Compute parameters: $\alpha, \beta, \gamma, \xi$; ▷ According to Eq. 15
4 Compute $\mathbf{H}_o$. ▷ According to Eq. 14

where α are independent geometric stiffness parameters. There exists orthogonality among $\{\mathrm{S}_0, \mathrm{S}_1, \mathrm{S}_2\}$ due to the orthogonality among $\{\mathbf{n}_1, \mathbf{m}_1, \mathbf{e}\}$ and $\{\mathbf{n}_2, \mathbf{m}_2, \mathbf{e}\}$. Actually, they have significant implications:

- S_0 damps the bending modes, i.e. the change of a dihedral angle θ, due to the effects of both $\mathbf{q}_0\mathbf{q}_0^\top$ and $\mathbf{q}_1\mathbf{q}_1^\top$.
- S_1 damps the altitude-changing modes. According to $\nabla_\mathbf{x}h_1$ and $\nabla_\mathbf{x}h_2$, we obtain an equivalent expression of S_1, i.e. $\mathrm{S}_1 = h_1^{-2}\nabla_\mathbf{x}h_1\nabla_\mathbf{x}^\top h_1 + h_2^{-2}\nabla_\mathbf{x}h_2\nabla_\mathbf{x}^\top h_2$, which represents a stiffness matrix for altitude changes.
- S_2 damps the barycentric sliding modes, i.e. non-uniform scaling along $\mathbf{e}$, and S_3 damps undesirable scaling orthogonal to $\mathbf{e}$. $\nabla\omega_1$ and $\nabla\omega_2$ contain $\mathbf{s} \otimes \mathbf{m}_1$ and $\mathbf{s} \otimes \mathbf{m}_2$ which have influence on $[h_1, h_2]$ and θ. If eliminating the effects of $\mathbf{m}_1$ and $\mathbf{m}_2$, we obtain an approximated expression of S_2, i.e. $\mathrm{S}_2 \approx l^2\left(h_1^{-2}\nabla_\mathbf{x}\omega_1\nabla_\mathbf{x}^\top\omega_1 + h_2^{-2}\nabla_\mathbf{x}\omega_2\nabla_\mathbf{x}^\top\omega_2\right)$, which represents a stiffness matrix for changes of barycentric weights.

4.3.3 Adaptive Parameters. However, determining the appropriate values for the intensity of these geometric stiffness can be challenging. Fortunately, we have successfully constructed an analytic eigensystem for the bending Hessian $\mathbf{H}$. We observe that the four geometric stiffness terms are already contained in $\mathbf{Z}\mathbf{Z}^\top$ and their coefficients can be extracted from the diagonal of $\mathbf{F}'$. To be conservative, we choose the four parameters to be

$$\begin{aligned}
\alpha_0 &= \max(\mathbf{F}'_{00}, \mathbf{F}'_{11}) - p, \quad & \alpha_1 &= \max(\mathbf{F}'_{22}, \mathbf{F}'_{33}),\\
\alpha_2 &= \max(\mathbf{F}'_{66}, \mathbf{F}'_{77}), & \alpha_3 &= \max(\mathbf{F}'_{44}, \mathbf{F}'_{55}).
\end{aligned} \tag{15}$$

Since these parameters are adaptively determined based on eigenvalues, they will be zero when a dihedral element is at the reference state. By using **F**-based adaptive parameters, our AOGS not only enhances the stability of simulation of thin plates with high bending-membrane ratios, as shown in Fig. 7(d), but also produces little artificial damping for simulation with low bending-membrane ratios, as shown in Fig. 1(e, j) and Fig. 16(b).

4.4 Compression Stiffness Adjustment (CSA)

Our AOGS is effective in suppressing rapid over-stretching and over-compression caused by large bending forces in simulations with a high BMR, as illustrated in Fig. 10. However, our AOGS only modifies the energy Hessian and does not affect the bending force. After applying our geometric stiffness, compressed dihedral elements can be difficult to recover due to the large damping for in-plane deformation. This is because the magnitude of both bending stiffness and geometric stiffness increases rapidly and nonlinearly as the altitudes of a dihedral element decrease. While the membrane stiffness remains constant for a linear model, the bending stiffness is

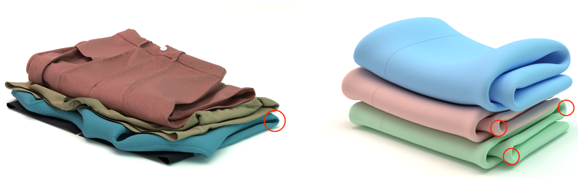

(a) Folded clothes (b) Folded layers

Fig. 8. Two multilayer folding examples. (a) Three clothes are sequentially folded and layered. The T-shirt on the bottom is the same one in Fig. 1(a) which has a high BMR. (b) Three folded layers with the same high BMR. When using the Gauss-Newton approximation to fix the indefiniteness issue, unstable oscillations are observed in the areas indicated by the red circles. In contrast, our AOGS produces stable simulation results without oscillations.

inversely proportional to the square of the hinge altitudes. However, even with low stretching stiffness, thin materials such as cloth are still not easy to compress [Choi and Ko 2002; Volino et al. 1995]. Thus, using a linear model to simulate compression resistance is unsuitable for thin materials. On the contrary, employing a nonlinear model such as the stabilized Neo-Hookean model [Smith et al. 2018] can generate sufficient resistance for compression. However, this approach requires multiple nonlinear iterations with step-length line-searching to ensure stability. Illustrated by Fig. 10(c), the combination of Gauss-Newton approximation for bending and Neo-Hookean for membrane results in simulation instability when using only one Newton's iteration strategy. Similarly, as displayed in Fig. 10(f), combining AOGS with Neo-Hookean leads to pronounced oscillations.

Choi and Ko [2002] presented a nonlinear compression model to handle the post-buckling when a spring is compressed. To address this issue, we suggest adjusting the stiffness of resistance for compression using a nonlinear function that is also inversely proportional to the square of the in-plane compression strain r. For as little coupling between membrane deformation and bending deformation as possible, we continue to use a linear model for stretching so that a nonlinear model for compression has negligible effects on the overall elasticity behavior. This yields the relation between the magnitude of resistance force for in-plane deformation and the principle strain r, i.e.

$$\begin{cases} f_m = K_m(r-1), & if\ r \geq 1; \\ f_m = K_m(r-1)/r^2, & if\ r < 1, \end{cases} \tag{16}$$

in which K_m is the original membrane stiffness. f_m is C_1 continuous around the rest state $r = 1$, allowing for a smooth transfer between stretching and compression near the rest state.

The nonlinear compression stiffness is helpful in avoiding instability caused by over-compression in simulations of thin materials with high bending-membrane ratios, such as clothing made of scuba fabrics. However, for most thin materials with low bending-membrane ratios, applying the nonlinear compression stiffness adjustment may worsen the locking issue. High and low bending-membrane ratios are both common in interactive apparel design simulations, so a criterion must be established to invoke the nonlinear compression stiffness adjustment. In the study of thin materials, continuum materials typically adhere to the Kirchhoff-Love thin plate theory [Timoshenko et al. 1959], which states that the bending and membrane rigidity of a thin plate with Young's modulus Y, Poisson's ratio v, and thickness h are denoted by

$$D = \frac{h^3 Y}{12(1-v^2)} \quad and \quad K = \frac{hY}{1-v^2}, \tag{17}$$

respectively. Thus, the bending-membrane ratio of a Kirchhoff-Love thin plate is only related to its thickness, i.e. BMR: $D/K = h^2/12$. We use BMR x1: $1e^{-6}/12$ to represent a Kirchhoff-Love plate with a thickness of 1 mm. Given a BMR xN, the corresponding thickness is $\sqrt{N}$ mm. For example, BMR x16 corresponds to 4 mm.

In our experiments, as illustrated in Fig. 5 and Fig. 17, we have observed that **H**-projection, **F**-projection and the Gauss-Newton approximation are stable when simulating Kirchhoff-Love thin plates. Based on this observation, we suggest using the Kirchhoff-Love ratio as a criterion to determine when to apply the nonlinear compression stiffness adjustment. Using Eq. 17, we can calculate a compression stiffness $K_{kl} = 12h^{-2}D$ that satisfies the Kirchhoff-Love thin plate theory in terms of bending and compression. Once the linear compression stiffness falls below K_{kl}, the nonlinear compression stiffness adjustment will be invoked. To ensure that materials with extremely low compression stiffness receive enough resistance for compression quickly, we propose linearly interpolating the compression stiffness between K_m and K_{kl} when compression occurs. By combining this with the nonlinear expression in Eq. 16, we obtain the final expression for adjusting compression stiffness,

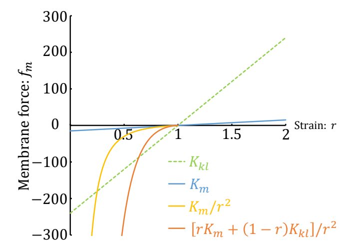

Fig. 9. Nonlinear compression stiffness.

$$\begin{cases} f_m = K_m(r-1), & if\ K_m \geq K_{kl}; \\ f_m = [rK_m + (1-r)K_{kl}](r-1)/r^2, & if\ K_m < K_{kl}. \end{cases} \tag{18}$$

As depicted in Fig. 9, f_m is also C_1 continuous at $r = 1$. As shown in Fig 10(e), we demonstrate the effectiveness of this approach in eliminating geometry degeneracy caused by over-compression. Using the Kirchhoff-Love ratio as a criterion provides an useful approach to balance stability and accuracy.

5 RESULTS

To demonstrate the effectiveness of our methods, we adopt a single Newton's iteration with a large time step 1/30s, which is a commonly used strategy [Baraff and Witkin 1998] for implicit time integration. To solve linear systems to single-precision float-point accuracy, we use a preconditioned CG method with 3×3 block diagonal matrices for preconditioning. The PCG algorithm stops once the L_2 residual norm is below $1e^{-5}$. To eliminate nonlinearity arising from hyperelasticity, we adopt Baraff-Witkin's linear elasticity model [Baraff and Witkin 1998] for in-plane deformation of unstructured triangle meshes, while our stabilized DAB models handle

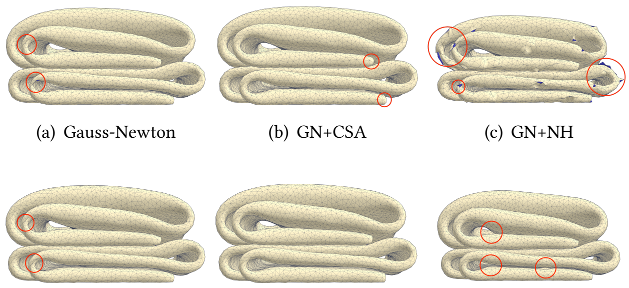

(a) Gauss-Newton (b) GN+CSA (c) GN+NH

(d) AOGS (e) AOGS+CSA (f) AOGS+NH

Fig. 10. A folding example of two layers simulated using only one Newton's iteration. (a) When using the Gauss-Newton approximation, oscillations and over-compression occur at the corners indicated by the red circles. (b) By applying our CSA, over-compression can be eliminated but oscillation still persists. However, when (d) our AOGS is utilized, the simulation becomes stable without any oscillation. Nevertheless, over-compression remains a problem. A nonlinear membrane model, such as (c, f) Neo-Hookean, results in simulation instability. By combining our AOGS and CAS, both over-compression and oscillation are eliminated.

out-of-plane deformation. All of our experiments are performed on a PC with an Intel Core i9-12900K 3.20GHz CPU on 16 cores, 64GB of RAM, and an NVIDIA GeForce GTX 3090 GPU. We evaluate the effectiveness of our methods using challenging examples. As listed in Table. 2, the material properties, including bending stiffness and membrane stiffness, of all examples are given.

5.1 Performance Evaluation

There are multiple methods to address the indefiniteness issue of DAB models, including the Gauss-Newton approximation, the Levenberg-Marquardt algorithm (LMA), the **H**-projection, and our proposed **F**-projection and AOGS. We have qualitatively assessed their stability by twisting and compressing cylinders in Fig. 5 and Fig. 7. Moreover, we quantitatively evaluate their performance in terms of solving linear systems and optimizing the nonlinear time-integration energy during the quasistatic process of a highly deformed armadillo (Fig. 13(b)) recovering to its reference state (Fig. 13(a)).

5.1.1 Convergence of solving linear systems. In the quasistatic simulation, a linear system needs to be solved at each Newton's iteration. The strategy used to construct a positive semi-definite bending energy Hessian can affect the convergence of a block-diagonal preconditioned CG method for solving the linear system. Fig. 11 shows that our AOGS achieves the best convergence in terms of both relative residual and energy errors.

5.1.2 Convergence of optimizing nonlinear energy. When performing a quasistatic simulation of a heavily deformed armadillo and utilizing multiple Newton's iterations to search for a nonlinear solution, a good bending Hessian strategy is crucial for achieving fast convergence with respect to nonlinear energy decrease. Fig. 12 demonstrates that our AOGS converges the fastest and always maintains a stable step length of one. Although LMA-0.5 outperforms

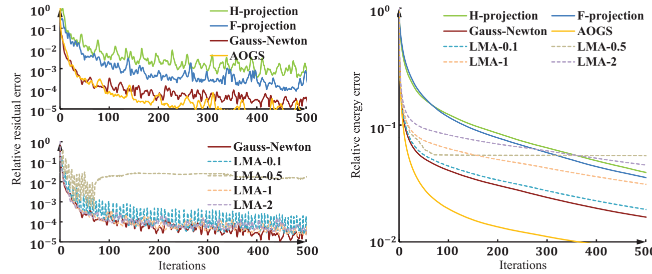

Fig. 11. Convergence of solving a linear system using PCG.

our AOGS after 10 iterations, determining the optimal damping parameter of the LMA can be challenging.

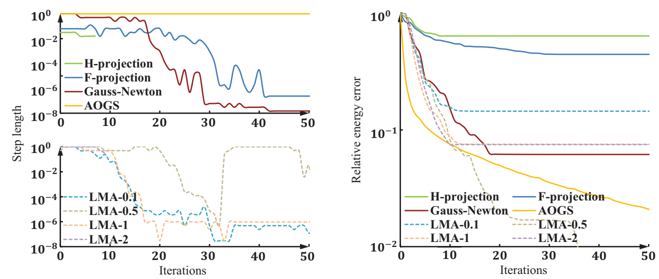

Fig. 12. Convergence of the nonlinear quasistatic simulation.

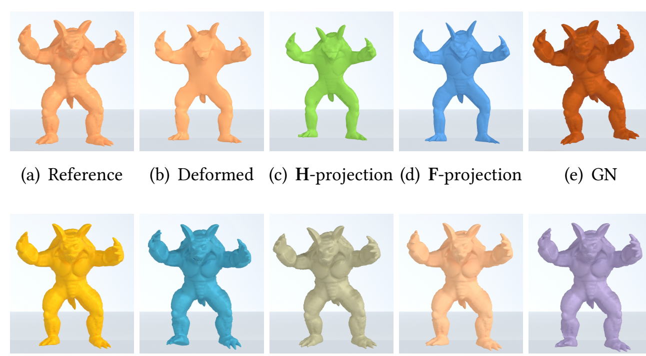

(a) Reference (b) Deformed (c) **H**-projection (d) **F**-projection (e) GN

(f) AOGS (g) LMA-0.1 (h) LMA-0.5 (i) LMA-1 (j) LMA-2

Fig. 13. (a) An armadillo modeled by triangular surface mesh is at its reference state. In the heavily deformed state (b), it stores large bending energy and contains many geometry degeneracies. When using different Hessian strategies in the quasistatic simulation, the armadillo displays different statuses at the 30th iteration.

5.1.3 Nonlinear Methods. While ensuring stability in nonlinear simulations can be achieved through small step lengths and line-searching methods, approaches that guarantee stability in linearly approximated simulations with only one Newton's iteration are rare. Our proposed methods provide an effective solution for enhancing the stability of widely used DAB models in linear simulations and

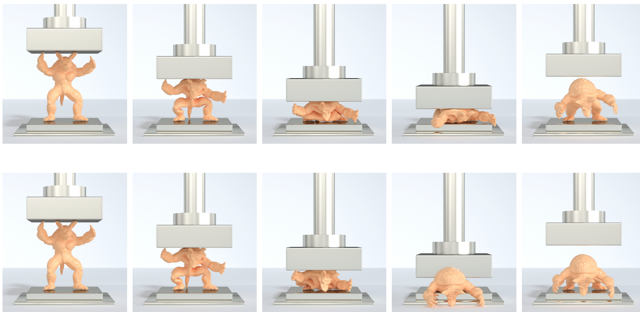

Fig. 14. A plastic armadillo is squeezed. At each frame, the total advancing step length is set as one. The first row is produced by using only one Newton's iteration with our AOGS, while the second row is results by using multiple Newton's iteration with Gauss-Newton approximation.

improving convergence in nonlinear simulations. In order to assess the performance benefits of our approach, we conducted a comparative analysis involving various nonlinear methods. This evaluation was carried out under the condition that the sum of step lengths across multiple nonlinear iterations within each frame equated to 1. In the process of simulating the deformation of a plastic armadillo in Fig 14, both Newton's method and the Stable Constrained Dynamics (SCD) [Tournier et al. 2015] with our AOGS takes only a single iteration to achieve the targeted advancing step length of 1. When comparing SCD to Newton's method, the only difference is that SCD approximates the computation of dihedral angle constraints using a first-order approach, which has negligible effect on the solution. Therefore, they produce similar results as displayed in the first row of Fig. 14. In the case where the armadillo experiences compression, Newton's method with the Gauss-Newton approximation demands approximately 60 iterations to attain the desired advancing step length of 1. However, our exploration extended beyond these methods. Regrettably, our attempts to utilize the nonlinear conjugate gradient and eXtended Position-Based Dynamics (XPBD) to simulate the armadillo's deformation yielded unsuccessful outcomes for this specific example.

5.2 Artificial Damping

Andrews et al. [2017] highlighted in their work that inappropriate geometric stiffness can introduce artificial damping and energy dissipation into dynamic simulations. In our folding examples, as shown in Fig. 8, we observe the difference between results obtained using our AOGS and the Gauss-Newton approximation. To assess the side effects of artificial damping of our AOGS, we conducted a dynamic simulation of five plates with increasing resolutions from far to near as shown in Fig. 15. To reduce the influence of numerical damping from implicit time integration, we use a small time step $1/300\ s$ in the simulation. We apply four different Hessian strategies to model bending deformation. When the bending stiffness is low, all four methods produce almost no artificial damping and are resolution-independent. However, only the Gauss-Newton approximation remains consistently resolution-independent as the bending stiffness increases. The other three methods produce increasingly more artificial damping as mesh resolution and bending stiffness increase. Nonetheless, our AOGS produces less artificial damping than the **H**-projection and **F**-projection, as demonstrated in our video. It is important to note that the Gauss-Newton approximation can result in underdamped results due to the absence of geometric stiffness. This can be observed in Fig. 16, where the pleated skirt simulated using the Gauss-Newton approximation exhibits dramatic swinging, while the result of our AOGS appears more plausible.

(a) **H**-projection (b) **F**-projection (c) Gauss-Newton (d) AOGS

Fig. 15. Five plates with increasing mesh resolutions from far(16mm) to near(1mm) are fixed on one end. They are placed at the same height and drop simultaneously. In this example with low bending stiffness, all four methods produce nearly the same result without artificial damping.

(a) Gauss-Newton (b) AOGS

Fig. 16. In the pleated skirt example, which features many folds where the bending stiffness is not continuous, both the Gauss-Newton approximation and our AOGS produce stable simulations without much artificial damping. However, when comparing the results at a specific frame, the result of (a) the Gauss-Newton approximation exhibits significant swinging motion. On the other hand, the result of (b) our AOGS appears more plausible and realistic.

5.3 Bending-membrane Ratio

In the realm of thin materials, the dominant physical behaviors are in-plane membrane elasticity and out-of-plane bending deformations. This interplay is depicted in Fig. 1, where variations in the combination of membrane and bending properties yield distinct simulation outcomes for the same T-shirt. In practical scenarios, thin materials may exhibit either low membrane stiffness, rendering them prone to stretching, or high membrane stiffness, making them resistant to deformation. Similarly, these materials could possess low bending stiffness, allowing easy curvature, or high bending stiffness, resulting in curvature resistance.

The bending-membrane ratio (BMR) quantifies the relative interplay between these factors and mirrors the material thickness. Generally, most realistic thin materials exhibit a low BMR. As shown in Fig. 17, existing methods can also produce stable simulation results. However, certain exceptional materials like specific scuba fabrics or composite materials can exhibit a high BMR. As shown in Fig. 8(a), there are oscillations on the folded scuba T-shirt. Importantly, DAB models are decoupled from membrane constitutive models. For user friendliness and convenience, we empower users to independently fine-tune bending and membrane parameters without a deep understanding of Kirchhoff-Love theory or real-world material parameters. Consequently, it becomes straightforward to create some non-physical material parameters, even those with high BMRs. Even so, maintaining simulation stability without compromising the interactive experience remains paramount.

(a) Exact Hessian (b) **H**-projection (c) **F**-projection (d) GN (e) AOGS

Fig. 17. A cylinder thin plate with a low BMR x1. Although the exact Hessian is indefinite, it produces stable simulation in this case.

Illustrated in Fig. 7, 8, 10, we have showcased the efficacy of our proposed orthotropic geometric stiffness (AOGS) and compression stiffness adjustment (CSA) in stabilizing simulation of thin materials using only one Newton's iteration with PCG as a linear solver. In combination with a linear membrane model, such as the Baraff-Witkin's model, our method facilitates the progression of Newton's iterations without the computational overhead of expensive line searches. This integration ensures the maintenance of interactive fluidity and responsiveness. Nonetheless, we must acknowledge that the advantages conferred by our approach in scenarios featuring a low BMR might not be as pronounced as those in high BMR cases. In the examples involving a crushing coke can in Fig. 18, whether incorporating plasticity or not, we note that the Gauss-Newton approximation can similarly facilitate Newton's iterations without line searches. This outcome arises from the fact that adequate membrane stiffness can mitigate the adverse consequences stemming from the absence of significant bending geometric stiffness.

5.4 Different DAB Models

By default, we use *Discrete Shells* as the DAB model in previous examples to simulate bending deformation. However, our AOGS is not limited to *Discrete Shells*, as we have also applied it to other DAB models to improve their stability, including *Cubic Shells*, *Bridson's model* and *Tamstorf's model*. In the case of large bending deformation, simply omitting the indefinite dihedral angle Hessian **G** is inadequate for *Cubic Shells* and *Tamsforf's model* to ensure positive semi-definiteness because p in Eq. 2 can be negative. Additionally, *Tamstorf's model* is more unstable than others due to its unbounded bending energy. As shown in Fig. 19, our AOGS can enhance stability of different DAB models, allowing a highly deformed armadillo with many (near-) degenerate geometries to stably recover to its reference state.

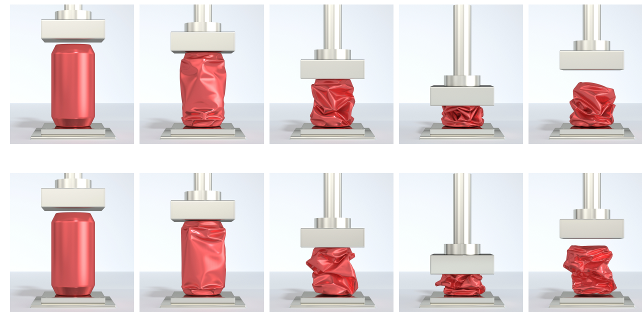

Fig. 18. An example of crushing coke cans. The can in the first row is without plasticity. The can in the second row is with plasticity. In this example, our AOGS exhibits little advantages over Gauss-Newton approximation, due to the strong membrane stiffness.

Table 2. Material parameters. D has unit $kg \cdot m^2 \cdot s^{-2}$ and K has unit $kg \cdot s^{-2}$. BMR is evaluated by $D/K = h^2/12$. The thickness corresponds to BMR xN is $\sqrt{N}$ mm, e.g. BMR x1, i.e. $1e^{-6}/12$, represents a Kirchhoff-Love plate with a thickness of 1 mm.

Examples	Fig. #	Bending: D	Membrane: K	BMR
T-shirt	Fig. 1(a)	$2e^{-5}$	15	x16
T-shirt	Fig. 1(b)	$2e^{-5}$	30	x8
T-shirt	Fig. 1(c)	$2e^{-5}$	60	x4
T-shirt	Fig. 1(d)	$2e^{-5}$	120	x2
T-shirt	Fig. 1(e)	$2e^{-5}$	240	x1
T-shirt	Fig. 1(i)	$1e^{-5}$	15	x8
T-shirt	Fig. 1(j)	$5e^{-6}$	15	x4
T-shirt	Fig. 1(k)	$2.5e^{-6}$	15	x2
T-shirt	Fig. 1(l)	$1.25e^{-6}$	15	x1
T-shirt	Fig. 8(a)	$2e^{-5}$	15	x16
Cylinder	Fig. 5	$2e^{-5}$	240	x1
Cylinder	Fig. 7	$2e^{-3}$	40	x600
Cylinder	Fig. 17	$1e^{-5}$	120	x1
Folded layers	Fig. 8(b)	$7e^{-5}$	15	x56
Folded layers	Fig. 10	$7e^{-5}$	15	x56
Armadillo	Fig. 13	$2e^{-3}$	160	x150
Armadillo	Fig. 14	$1e^{-4}$	160	x7.5
Pleated skirt	Fig. 16	$1e^{-3}$	100	x0.12
Coke can	Fig. 18	$5e^{-5}$	$1e^{4}$	x0.06

6 CONCLUSIONS, LIMITATIONS AND FUTURE WORK

This paper presents a concise matrix expression for the energy Hessian of dihedral angle based discrete bending models and proposes an innovative analytic expressions for the eigensystem of DAB models to address the indefiniteness issue. Based on the twelve motion modes of a dihedral element, we demonstrate that original geometric stiffness matrix of DAB models retains the undesirable altitude-changing modes and propose an orthotropic geometric stiffness model with adaptive parameters which retains the desirable bending modes and can improve simulation stability at degenerate geometries. Our method supports stable simulations of thin materials with a wide range of bending-membrane ratios. Nonetheless,

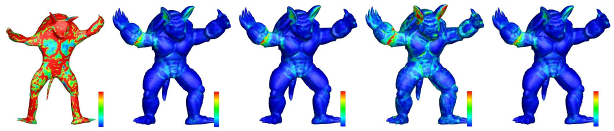

(a) Deformed (b) DS (c) CS (d) Bridson's (e) Tamstorf's

Fig. 19. This is an armadillo-shaped thin shell modeled by an unstructured triangular mesh. We perform a quasistatic simulation to minimize the inner potential energy of the armadillo from a heavily deformed state (a) to a equilibrium state. (b), (c), (d), and (e) are bending energy maps using four different DAB models with our AOGS after 3 quasistatic iterations. The red and blue regions represent the high and low bending energy, respectively.

artificial damping is noticeable when simulating high-resolution meshes with high bending stiffness. In addition, our compression stiffness adjustment inherits the property of Kirchhoff-Love thin plate that introduces some coupling between in-plane compression and out-of-plane bending. To further improve bending models for discrete surfaces, future work could focus on eliminating the influence of mesh tessellation on edge-based discrete bending models and addressing the well-known locking issue when the bending-membrane ratio is low.

ACKNOWLEDGMENTS

We wish to thank reviewers for valuable comments and the digital content team at Style3D for helping with rendering and scene creation. We also thank Zeagle Liu and Tao Yu for proofreading and Tianqi Gao for encouragement and support. This work was partly supported by Key R&D Program of Zhejiang (No. 2023C01047).

REFERENCES

Sheldon Andrews, Marek Teichmann, and Paul G Kry. 2017. Geometric Stiffness for Real-time Constrained Multibody Dynamics. *Computer Graphics Forum* 36, 2 (2017), 235–246.

David Baraff and Andrew Witkin. 1998. Large Steps in Cloth Simulation. In *Proceedings of the 25th Annual Conference on Computer Graphics and Interactive Techniques (SIGGRAPH '98)*. Association for Computing Machinery, New York, NY, USA, 43–54.

Miklós Bergou, Saurabh Mathur, Max Wardetzky, and Eitan Grinspun. 2007. TRACKS: Toward Directable Thin Shells. *ACM Trans. Graph.* 26, 3 (jul 2007), 50–es.

Miklos Bergou, Max Wardetzky, David Harmon, Denis Zorin, and Eitan Grinspun. 2006a. Discrete Quadratic Curvature Energies. In *ACM SIGGRAPH 2006 Courses* (Boston, Massachusetts) *(SIGGRAPH '06)*. Association for Computing Machinery, New York, NY, USA, 20–29.

Miklos Bergou, Max Wardetzky, David Harmon, Denis Zorin, and Eitan Grinspun. 2006b. A Quadratic Bending Model for Inextensible Surfaces. In *Proceedings of the Fourth Eurographics Symposium on Geometry Processing* (Cagliari, Sardinia, Italy) *(SGP '06)*. Eurographics Association, Goslar, DEU, 227–230.

Alexander I. Bobenko and Peter Schröder. 2005. Discrete Willmore Flow. In *ACM SIGGRAPH 2005 Courses* (Los Angeles, California) *(SIGGRAPH '05)*. Association for Computing Machinery, New York, NY, USA, 5–es.

R. Bridson, S. Marino, and R. Fedkiw. 2003. Simulation of Clothing with Folds and Wrinkles. In *Proceedings of the 2003 ACM SIGGRAPH/Eurographics Symposium on Computer Animation* (San Diego, California) *(SCA '03)*. Eurographics Association, Goslar, DEU, 28–36.

Peter B Canham. 1970. The minimum energy of bending as a possible explanation of the biconcave shape of the human red blood cell. *Journal of theoretical biology* 26, 1 (1970), 61–81.

Hsiao-Yu Chen, Arnav Sastry, Wim M. van Rees, and Etienne Vouga. 2018. Physical Simulation of Environmentally Induced Thin Shell Deformation. *ACM Trans. Graph.* 37, 4, Article 146 (jul 2018), 13 pages.

Zhen Chen, Hsiao-Yu Chen, Danny M. Kaufman, Mélina Skouras, and Etienne Vouga. 2021. Fine Wrinkling on Coarsely Meshed Thin Shells. *ACM Trans. Graph.* 40, 5, Article 190 (aug 2021), 32 pages.

Kwang-Jin Choi and Hyeong-Seok Ko. 2002. Stable but Responsive Cloth. *ACM Trans. Graph. (SIGGRAPH)* 21, 3 (July 2002), 604–611.

David Cohen-Steiner and Jean-Marie Morvan. 2003. Restricted Delaunay Triangulations and Normal Cycle. In *Proceedings of the Nineteenth Annual Symposium on Computational Geometry* (San Diego, California, USA) *(SCG '03)*. Association for Computing Machinery, New York, NY, USA, 312–321.

Robert D Cook. 1994. *Modeling for Stress Analysis.* New York: Wiley.

Xudong Feng, Wenchao Huang, Weiwei Xu, and Huamin Wang. 2022. Learning-Based Bending Stiffness Parameter Estimation by a Drape Tester. *ACM Trans. Graph.* 41, 6, Article 221 (nov 2022), 16 pages.

Akash Garg, Eitan Grinspun, Max Wardetzky, and Denis Zorin. 2007. Cubic Shells. In *Proceedings of the 2007 ACM SIGGRAPH/Eurographics Symposium on Computer Animation* (San Diego, California) *(SCA '07)*. Eurographics Association, Goslar, DEU, 91–98.

Yotam Gingold, Adrian Secord, Jefferson Y. Han, Eitan Grinspun, and Denis Zorin. 2004. *A Discrete Model for Inelastic Deformation of Thin Shells.* Technical Report.

Rony Goldenthal, David Harmon, Raanan Fattal, Michel Bercovier, and Eitan Grinspun. 2007. Efficient simulation of inextensible cloth. *ACM Trans. Graph. (SIGGRAPH)* 26, 3, Article 49 (July 2007).

Seth Green, George Turkiyyah, and Duane Storti. 2002. Subdivision-based Multilevel Methods for Large Scale Engineering Simulation of Thin Shells. In *Proceedings of SMA* (Saarbrücken, Germany). 265–272.

Eitan Grinspun. 2005. A Discrete Model of Thin Shells. In *ACM SIGGRAPH 2005 Courses* (Los Angeles, California) *(SIGGRAPH '05)*. Association for Computing Machinery, New York, NY, USA, 4–es.

Eitan Grinspun. 2006. Discrete Differential Geometry: An Applied Introduction. In *ACM SIGGRAPH 2006 Courses* (Boston, Massachusetts) *(SIGGRAPH '06)*. Association for Computing Machinery, New York, NY, USA.

Eitan Grinspun, Yotam Gingold, Jason Reisman, and Denis Zorin. 2006. Computing discrete shape operators on general meshes. In *Computer Graphics Forum*, Vol. 25. Wiley Online Library, 547–556.

Eitan Grinspun, Anil N. Hirani, Mathieu Desbrun, and Peter Schröder. 2003. Discrete Shells. In *Proceedings of the 2003 ACM SIGGRAPH/Eurographics Symposium on Computer Animation* (San Diego, California) *(SCA '03)*. Eurographics Association, Goslar, DEU, 62–67.

Qi Guo, Xuchen Han, Chuyuan Fu, Theodore Gast, Rasmus Tamstorf, and Joseph Teran. 2018. A Material Point Method for Thin Shells with Frictional Contact. *ACM Trans. Graph.* 37, 4, Article 147 (jul 2018), 15 pages.

Wolfgang Helfrich. 1973. Elastic properties of lipid bilayers: theory and possible experiments. *Zeitschrift für Naturforschung c* 28, 11-12 (1973), 693–703.

Danny M. Kaufman, Rasmus Tamstorf, Breannan Smith, Jean-Marie Aubry, and Eitan Grinspun. 2014. Adaptive Nonlinearity for Collisions in Complex Rod Assemblies. *ACM Trans. Graph.* 33, 4, Article 123 (jul 2014), 12 pages.

Mark Meyer, Mathieu Desbrun, Peter Schröder, and Alan H Barr. 2003. Discrete differential-geometry operators for triangulated 2-manifolds. In *Visualization and mathematics III.* Springer, 35–57.

Rahul Narain, Tobias Pfaff, and James F. O'Brien. 2013. Folding and Crumpling Adaptive Sheets. *ACM Trans. Graph. (SIGGRAPH)* 32, 4, Article 51 (July 2013), 8 pages.

Konrad Polthier et al. 2002. *Polyhedral surfaces of constant mean curvature.* Ph. D. Dissertation. Citeseer.

E Rank, A Düster, V Nübel, K Preusch, and OT Bruhns. 2005. High order finite elements for shells. *Computer Methods in Applied Mechanics and Engineering* 194, 21-24 (2005), 2494–2512.

Olivier Rémillard and Paul G. Kry. 2013. Embedded Thin Shells for Wrinkle Simulation. *ACM Trans. Graph.* 32, 4, Article 50 (jul 2013), 8 pages.

Victor Romero, Mickaël Ly, Abdullah Haroon Rasheed, Raphaël Charrondière, Arnaud Lazarus, Sébastien Neukirch, and Florence Bertails-Descoubes. 2021. Physical Validation of Simulators in Computer Graphics: A New Framework Dedicated to Slender Elastic Structures and Frictional Contact. *ACM Trans. Graph.* 40, 4, Article 66 (jul 2021), 19 pages.

Breannan Smith, Fernando De Goes, and Theodore Kim. 2018. Stable Neo-Hookean Flesh Simulation. *ACM Trans. Graph.* 37, 2, Article 12 (mar 2018), 15 pages. https://doi.org/10.1145/3180491

Breannan Smith, Fernando De Goes, and Theodore Kim. 2019. Analytic Eigensystems for Isotropic Distortion Energies. *ACM Trans. Graph.* 38, 1, Article 3 (feb 2019), 15 pages. https://doi.org/10.1145/3241041

John M. Sullivan. 2005. Curvature Measures for Discrete Surfaces. In *ACM SIGGRAPH 2005 Courses* (Los Angeles, California) *(SIGGRAPH '05)*. Association for Computing Machinery, New York, NY, USA, 3–es.

John M Sullivan. 2008. Curvatures of smooth and discrete surfaces. (2008), 175–188.

Rasmus Tamstorf and Eitan Grinspun. 2013. Discrete bending forces and their Jacobians. *Graphical models* 75, 6 (2013), 362–370.

Joseph Teran, Eftychios Sifakis, Geoffrey Irving, and Ronald Fedkiw. 2005. Robust Quasistatic Finite Elements and Flesh Simulation. In *Proceedings of the 2005 ACM SIGGRAPH/Eurographics Symposium on Computer Animation* (Los Angeles, California) *(SCA '05)*. Association for Computing Machinery, New York, NY, USA, 181–190.

Stephen Timoshenko, Sergius Woinowsky-Krieger, et al. 1959. *Theory of plates and shells*. Vol. 2. McGraw-hill New York.

Maxime Tournier, Matthieu Nesme, Benjamin Gilles, and François Faure. 2015. Stable Constrained Dynamics. *ACM Trans. Graph. (SIGGRAPH)* 34, 4, Article 132 (July 2015), 10 pages.

Pascal Volino, Martin Courchesne, and Nadia Magnenat Thalmann. 1995. Versatile and Efficient Techniques for Simulating Cloth and Other Deformable Objects. In *Proceedings of the 22nd Annual Conference on Computer Graphics and Interactive Techniques (SIGGRAPH '95)*. Association for Computing Machinery, New York, NY, USA, 137?144.

Pascal Volino and Nadia Magnenat-Thalmann. 2006. Simple Linear Bending Stiffness in Particle Systems. In *Proceedings of the 2006 ACM SIGGRAPH/Eurographics Symposium on Computer Animation* (Vienna, Austria) *(SCA '06)*. Eurographics Association, Goslar, DEU, 101–105.

M Wacker and B Thomaszewski. 2006. Bending models for thin flexible objects. In *WSCG Short Communication proceedings*. Václav Skala-UNION Agency.

Huamin Wang, James F. O'Brien, and Ravi Ramamoorthi. 2011. Data-Driven Elastic Models for Cloth: Modeling and Measurement. *ACM Trans. Graph. (SIGGRAPH)* 30, 4, Article 71 (July 2011), 12 pages.

Max Wardetzky, Miklós Bergou, David Harmon, Denis Zorin, and Eitan Grinspun. 2007. Discrete quadratic curvature energies. *Computer Aided Geometric Design* 24, 8-9 (2007), 499–518.

Botao Wu, Zhendong Wang, and Huamin Wang. 2022. A GPU-Based Multilevel Additive Schwarz Preconditioner for Cloth and Deformable Body Simulation. *ACM Trans. Graph.* 41, 4, Article 63 (jul 2022), 14 pages. https://doi.org/10.1145/3528223.3530085

Joanne Yip and Sun-Pui Ng. 2008. Study of three-dimensional spacer fabrics:: Physical and mechanical properties. *Journal of materials processing technology* 206, 1-3 (2008), 359–364.

Yuan Zhang, Hong Hu, Yordan Kyosev, and Yanping Liu. 2020. Finite element modeling of 3D spacer fabric: effect of the geometric variation and amount of spacer yarns. *Composite Structures* 236 (2020), 111846.

Olgierd Cecil Zienkiewicz, Robert Leroy Taylor, and Robert Leroy Taylor. 2000. *The finite element method: solid mechanics*. Vol. 2. Butterworth-heinemann.

A DERIVATION OF DIHERAL ANGLE HESSIAN

When a dihedral element has bending deformation, i.e. the dihedral angle difference is not zero, the dihedral angle Hessian $\mathbf{G}$ in Eq. 4 is required to compute the energy Hessian. As depicted in Fig. 2, the shape of a dihedral element is determined by six pivotal independent variables $[\theta, l, h_1, h_2, \omega_1, \omega_2]$. Their gradients with respect to positions $\mathbf{x}$ are helpful for calculating the dihedral angle Hessian $\mathbf{G}$. We summarize them as

$$\begin{aligned}
&\nabla\theta = \mathbf{t}_1 \otimes \mathbf{n}_1 + \mathbf{t}_2 \otimes \mathbf{n}_2, && \nabla l = -l\mathbf{s} \otimes \mathbf{e}, \\
&\nabla h_1 = -h_1\mathbf{t}_1 \otimes \mathbf{m}_1, && \nabla\omega_1 = l^{-1}h_1\left(\mathbf{t}_1 \otimes \mathbf{e} + \mathbf{s} \otimes \mathbf{m}_1\right), \\
&\nabla h_2 = -h_2\mathbf{t}_2 \otimes \mathbf{m}_2, && \nabla\omega_2 = l^{-1}h_2\left(\mathbf{t}_2 \otimes \mathbf{e} + \mathbf{s} \otimes \mathbf{m}_2\right),
\end{aligned} \tag{19}$$

in which $\mathbf{s}$, $\mathbf{t}_1$ and $\mathbf{t}_2$ have been defined in Table 1. Please refer to [Tamstorf and Grinspun 2013] for detailed derivation of $\nabla\theta$. The derivations of gradients of the other five variables are simple so we do not present them here in detail. Tamstorf and Grinspun [2013] have presented $\mathbf{G}$ term by term. However, their expression is tedious and we would like to reformulate it in matrix format so that we can reveal the importance of the gradients in Eq. 19 for $\mathbf{G}$.

In matrix format, we get $\mathbf{G} = \nabla(\mathbf{t}_1 \otimes \mathbf{n}_1) + \nabla(\mathbf{t}_2 \otimes \mathbf{n}_2)$, in which

$$\begin{aligned}
\nabla(\mathbf{t}_1 \otimes \mathbf{n}_1) &= \nabla\mathbf{t}_1 \otimes \mathbf{n}_1^\top + \mathbf{t}_1^\top \otimes \nabla\mathbf{n}_1 \\
\nabla(\mathbf{t}_2 \otimes \mathbf{n}_2) &= \nabla\mathbf{t}_2 \otimes \mathbf{n}_2^\top + \mathbf{t}_2^\top \otimes \nabla\mathbf{n}_2.
\end{aligned} \tag{20}$$

Therefore, the gradients of $\mathbf{t}_1$, $\mathbf{t}_2$, $\mathbf{n}_1$ and $\mathbf{n}_2$ are needed. In isometric simulation, $\mathbf{t}_1$ and $\mathbf{t}_2$ are constant. However, if they are variant during non-isometric simulation, their derivatives

$$\begin{aligned}
\nabla\mathbf{t}_1 &= h_1^{-1}(l\mathbf{s}^\top \otimes \nabla\omega_1 - \mathbf{t}_1^\top \otimes \nabla h_1) \\
\nabla\mathbf{t}_2 &= h_2^{-1}(l\mathbf{s}^\top \otimes \nabla\omega_2 - \mathbf{t}_2^\top \otimes \nabla h_2),
\end{aligned} \tag{21}$$

should be taken into consideration. The gradient of triangle normals are borrowed from [Tamstorf and Grinspun 2013], which are

$$\begin{aligned}
\nabla\mathbf{n}_1 &= \mathbf{t}_1 \otimes (\mathbf{n}_1\mathbf{m}_1^\top) + \mathbf{s} \otimes (\mathbf{n}_1\mathbf{e}^\top), \\
\nabla\mathbf{n}_2 &= \mathbf{t}_2 \otimes (\mathbf{n}_2\mathbf{m}_2^\top) + \mathbf{s} \otimes (\mathbf{n}_2\mathbf{e}^\top).
\end{aligned} \tag{22}$$

Substituting Eq. 21 and Eq. 22 into Eq. 20 getting us

$$\begin{aligned}
\nabla(\mathbf{t}_1 \otimes \mathbf{n}_1) &= (\mathbf{t}_1\mathbf{t}_1^\top) \otimes \mathbf{A}_1 + (\mathbf{B}_1 + \mathbf{B}_1^\top) + (\mathbf{s}\mathbf{s}^\top) \otimes (\mathbf{m}_1\mathbf{n}_1^\top), \\
\nabla(\mathbf{t}_2 \otimes \mathbf{n}_2) &= (\mathbf{t}_2\mathbf{t}_2^\top) \otimes \mathbf{A}_2 + (\mathbf{B}_2 + \mathbf{B}_2^\top) + (\mathbf{s}\mathbf{s}^\top) \otimes (\mathbf{m}_2\mathbf{n}_2^\top),
\end{aligned} \tag{23}$$

where $\mathbf{A}_1 = \mathbf{m}_1\mathbf{n}_1^\top + \mathbf{n}_1\mathbf{m}_1^\top$ and $\mathbf{A}_2 = \mathbf{m}_2\mathbf{n}_2^\top + \mathbf{n}_2\mathbf{m}_2^\top \in \mathbb{R}^{3\times3}$, $\mathbf{B}_1 = (\mathbf{t}_1\mathbf{s}^\top) \otimes (\mathbf{e}\mathbf{n}_1^\top)$ and $\mathbf{B}_2 = (\mathbf{t}_2\mathbf{s}^\top) \otimes (\mathbf{e}\mathbf{n}_2^\top) \in \mathbb{R}^{12\times12}$. Let $\mathbf{C} = \mathbf{m}_1\mathbf{n}_1^\top + \mathbf{m}_2\mathbf{n}_2^\top \in \mathbb{R}^{3\times3}$, we can get $\mathbf{A}_1 + \mathbf{A}_2 = \mathbf{C} + \mathbf{C}^\top$. $\mathbf{C}$ have been proved symmetric by Tamstorf and Grinspun [2013]. Therefore, we have $\mathbf{C} = (\mathbf{A}_1 + \mathbf{A}_2)/2$. By reformulating Eq. 23, we get the final formula of the dihedral angle Hessian in Eq. 4.

B ANALYTIC EIGENSYSTEM

Our discovery of the analytic expression for the eigensystem of the energy Hessian of DAB models involves three key steps: the discovery of matrix $\mathbf{Z}$, the discovery of the intrinsic bending matrix $\mathbf{F}$, and the analytic eigensystem of $\mathbf{F}$.

B.1 The discovery of $\mathbf{Z}$

At the beginning of analyzing the eigensystem of the energy Hessian, we face considerable challenges and uncertainties. However, through a careful examination of the twelve motion modes described by Bridson et al. [2003], we discover that eight vectors, as presented in Eq. 6, recur consistently throughout our analysis. This discovery provide a significant impetus for us to pursue the development of analytic eigensystems for general DAB models, rather than relying the computationally expensive and numerically unstable SVD-based eigenvalue decomposition.

In Section. 4.2.1, we have comprehensively described the twelve motion modes of a dihedral element, and the corresponding displacement vectors for each mode are presented in Eq. 5. Although we initially attempted to construct the eigenvectors of $\mathbf{H}$ from $\boldsymbol{\nu}$, we encounter difficulties and are unable to achieve the desired outcome, though the four zero-eigenvalue eigenvectors have been found and the left eight $\boldsymbol{\nu}$s are orthogonal to each other. When we are going to give up, the result of $\mathbf{H}\boldsymbol{\nu}_i$ shed light on our path forward, which are

$$\begin{aligned}
&\mathbf{H}\boldsymbol{\nu}_4 = \mu g h_1^{-1}\left(\mathbf{s} \otimes \mathbf{n}_1\right) && \mathbf{H}\boldsymbol{\nu}_5 = \mu g h_2^{-1}\left(\mathbf{s} \otimes \mathbf{n}_2\right), \\
&\mathbf{H}\boldsymbol{\nu}_6 = \mu g h_1{}^{-1}\left(\mathbf{t}_1 \otimes \mathbf{n}_1\right) && \mathbf{H}\boldsymbol{\nu}_7 = \mu g h_2{}^{-1}\left(\mathbf{t}_2 \otimes \mathbf{n}_2\right), \\
&\mathbf{H}\boldsymbol{\nu}_8 = \mu h_1^{-1}\left(p\nabla\theta + g\mathbf{t}_1 \otimes \mathbf{m}_1\right) && \mathbf{H}\boldsymbol{\nu}_9 = \mu h_2^{-1}\left(p\nabla\theta + g\mathbf{t}_2 \otimes \mathbf{m}_2\right).
\end{aligned}$$

$$\begin{aligned}
\mathbf{H}\boldsymbol{\nu}_{10} = {}&\mu p l(\mathbf{t}_1^\top\mathbf{s} - \cos\theta\,\mathbf{t}_2^\top\mathbf{s})\nabla\theta + \mu g l\left[\mathbf{a}\otimes\mathbf{m}_1 + \mathbf{b}\otimes(\mathbf{A}_2\mathbf{n}_1)\right] + \\
&2\mu g l^{-1}\left(\mathbf{t}_1 + \mathbf{t}_2\right) \otimes \mathbf{e}, \\
\mathbf{H}\boldsymbol{\nu}_{11} = {}&\mu p l \sin\theta(\mathbf{t}_2^\top\mathbf{s})\nabla\theta + \mu g l\left[\mathbf{a}\otimes\mathbf{n}_1 + \mathbf{b}\otimes(\mathbf{A}_2\mathbf{m}_1)\right],
\end{aligned}$$

in which $\mathbf{a} = (\mathbf{t}_1^\top\mathbf{s})\mathbf{t}_1 + l^{-2}\mathbf{s}$ and $\mathbf{b} = (\mathbf{t}_2^\top\mathbf{s})\mathbf{t}_2 + l^{-2}\mathbf{s}$. An important observation from expressions of $\mathbf{H}\boldsymbol{\nu}_j$ ($j \in \{0, \ldots, 11\}$) is that there are eight independent vectors in Eq. 6 appearing repeatedly. The reason of why $\mathbf{t}_2 \otimes \mathbf{n}_2$, $\mathbf{t}_2 \otimes \mathbf{m}_2$, $\mathbf{s} \otimes \mathbf{n}_2$ and $\mathbf{s} \otimes \mathbf{m}_2$ are absent is that $\mathbf{n}_2$ and $\mathbf{m}_2$ are linearly dependent on $\mathbf{n}_1$ and $\mathbf{m}_1$, i.e. $\mathbf{n}_2 = -\cos\theta\mathbf{n}_1 + \sin\theta\mathbf{m}_1$ and $\mathbf{m}_2 = \sin\theta\mathbf{n}_1 + \cos\theta\mathbf{m}_1$. As a result, the matrix $\mathbf{Z} = \left[\boldsymbol{\zeta}_0, \ldots, \boldsymbol{\zeta}_8\right] \in \mathbb{R}^{12\times8}$ is composed of the eight $\boldsymbol{\zeta}$s in Eq. 6.

B.2 Intrinsic Bending Deformation

Furthermore, we discover $\mathbf{HZ} = \mathbf{ZC}$ where $\mathbf{C} \in \mathbb{R}^{8\times 8}$ is an important coefficient matrix. This revelation indicates that the column space of $\mathbf{Z}$ is an invariant subspace of $\mathbf{H}$ and $\mathbf{Z}$ is closely related to the corresponding eigenvectors, denoted as $\mathbf{E} = [\boldsymbol{\epsilon}_0, \dots, \boldsymbol{\epsilon}_{11}]$.

For any arbitrary vector $\boldsymbol{\nu} \in \mathbb{R}^{12}$, it can be easily verified that $\boldsymbol{\epsilon} = \mathbf{H}\boldsymbol{\nu} = \mathbf{Z}\boldsymbol{\gamma}$ where $\boldsymbol{\gamma} \in \mathbb{R}^8$ is a coefficient vector. Consequently, we can determine that $\boldsymbol{\epsilon}$ represents the general form of eigenvectors corresponding to nonzero eigenvalues. To ensure orthogonality between two different eigenvectors $\boldsymbol{\epsilon}_i$ and $\boldsymbol{\epsilon}_j$, we require $\boldsymbol{\epsilon}_i^\mathsf{T}\boldsymbol{\epsilon}_j = \boldsymbol{\gamma}_i^\mathsf{T}\mathbf{W}\boldsymbol{\gamma}_j = 0$, where $\mathbf{W} = \mathbf{Z}^\mathsf{T}\mathbf{Z}$ is positive-definite due to the full column rank of $\mathbf{Z}$. Since $\boldsymbol{\epsilon}$ is an eigenvector, we have $\mathbf{HZ}\boldsymbol{\gamma} = \lambda\mathbf{Z}\boldsymbol{\gamma}$, which leads to $\mathbf{ZC}\boldsymbol{\gamma} = \lambda\mathbf{Z}\boldsymbol{\gamma}$. Consequently, we can conclude that $\mathbf{C}\boldsymbol{\gamma} = \lambda\boldsymbol{\gamma}$, implying that the eigenvalues of $\mathbf{C}$ are also eigenvalues of $\mathbf{H}$ and $\boldsymbol{\gamma}$ is the eigenvector of $\mathbf{C}$. Hence, the orthogonality between eigenvectors gets us the following two conditions,

$$\begin{cases} \boldsymbol{\gamma}_i^\mathsf{T}\mathbf{W}\boldsymbol{\gamma}_j = 0 & \text{if } i \neq j, \\ \boldsymbol{\gamma}_i^\mathsf{T}\mathbf{C}\boldsymbol{\gamma}_j = 0 & \text{if } i \neq j. \end{cases} \tag{24}$$

Actually, there exists a close connection between $\mathbf{C}$ and $\mathbf{W}$, specifically $\mathbf{C} = \mathbf{FW}$, where $\mathbf{F}$ is a symmetric block diagonal matrix that is solely related to the current and reference dihedral angle, θ and $\bar{\theta}$. The detailed deduction process of $\mathbf{F}$ is tedious and can be found in the subsequent section, Section. B.3. Fundamentally, $\mathbf{F}$ represents the bending deformation of a dihedral element, while $\mathbf{W}$ represents the in-plane information of a dihedral element.

We have presented the analytic eigensystem of DAB models in our paper. A significant finding is that $\mathbf{F}$ typically has positive, negative and zero eigenvalues, with four of each, when a dihedral element is apart from its reference bending state. However, the eigensystem of $\mathbf{F}$ differs from the eigensystem of $\mathbf{H}$ due to the lack of orthogonality among the columns of $\mathbf{Z}$. Despite our attempts to derive the exact analytic eigensystem of $\mathbf{H}$ by utilizing Eq. 24, we were unsuccessful. Nevertheless, we have proven that $\mathbf{H}$ also typically has four positive and four negative eigenvalues, as well as four zero eigenvalues.

Proof. According to Eq. 7 and Eq. 10, we obtain a useful decomposition for the energy Hessian, namely $\mathbf{H} = \mu(\mathbf{ZE})\boldsymbol{\Lambda}(\mathbf{ZE})^\mathsf{T}$, in which $\mathbf{ZE} \in \mathbb{R}^{12\times 8}$ has full column rank. If the matrix $\mathbf{ZE}$ had orthogonal column vectors, we could easily conclude that $\mathbf{H}$ would have four positive and four negative eigenvalues, as $\boldsymbol{\Lambda}$ has four positive and four negative eigenvalues. However, $\mathbf{ZE}$ does not have orthogonal columns. By performing QR decomposition to $\mathbf{ZE}$, we obtain an matrix $\mathbf{Q} \in \mathbb{R}^{12\times 8}$ with orthogonal unit column vectors, i.e. $\mathbf{ZE} = \mathbf{QR}$ where $\mathbf{R} \in \mathbb{R}^{8\times 8}$ is a upper-triangular matrix with full rank. Consequently, we obtain another equivalent decomposition for the energy Hessian, i.e. $\mathbf{H} = \mu\mathbf{QTQ}^\mathsf{T}$, in which the matrix $\mathbf{T} = \mathbf{R}\boldsymbol{\Lambda}\mathbf{R}^\mathsf{T}$ has the same number of negative eigenvalues as $\boldsymbol{\Lambda}$, and the same applies to the number of positive eigenvalues. This results follows Sylvester's law of inertia, provided that $\mathbf{R}$ is an invertible matrix. Thus, we conclude that $\mathbf{H}$ also have the same numbers of negative eigenvalues and positive eigenvalues as $\boldsymbol{\Lambda}$. □

B.3 The discovery of F

Actually, the derivation of $\mathbf{F}$ is a nontrivial task. Specifically, we carefully deduce the following eight expressions that can be used to construct matrix $\mathbf{F}$. These expressions ultimately lead us to the important result, $\mathbf{HZ} = \mu\mathbf{ZFZ}^\mathsf{T}\mathbf{Z}$. Due to the full column rank of $\mathbf{Z}$, we ca further derive Eq. 7 and obtain the analytic expression for matrix $\mathbf{F}$.

$$\begin{aligned}
\mathbf{H}\boldsymbol{\zeta}_0 =& \mu p\left[\mathbf{t}_1^\mathsf{T}\mathbf{t}_1 - \cos\theta\left(\mathbf{t}_2^\mathsf{T}\mathbf{t}_1\right)\right]\left[\mathbf{t}_1\otimes\mathbf{n}_1 + \mathbf{t}_2\otimes(-\cos\theta\mathbf{n}_1 + \sin\theta\mathbf{m}_1)\right] + \\
& \mu g\left[\left(\mathbf{t}_1^\mathsf{T}\mathbf{t}_1\right)\mathbf{t}_1\otimes\mathbf{m}_1 + \left(\mathbf{t}_2^\mathsf{T}\mathbf{t}_1\right)\mathbf{t}_2\otimes(-\sin 2\theta\mathbf{n}_1 - \cos 2\theta\mathbf{m}_1)\right] + \\
& \mu g\left(\mathbf{s}^\mathsf{T}\mathbf{t}_1\right)\left[\mathbf{s}\otimes\left(-\frac{1}{2}\sin 2\theta\mathbf{n}_1 + \sin^2\theta\mathbf{m}_1\right) + (\mathbf{t}_1 - \cos\theta\mathbf{t}_2)\otimes\mathbf{e}\right], \\
\mathbf{H}\boldsymbol{\zeta}_1 =& \mu p\left[\mathbf{t}_1^\mathsf{T}\mathbf{t}_2 - \cos\theta\left(\mathbf{t}_2^\mathsf{T}\mathbf{t}_2\right)\right]\left[\mathbf{t}_1\otimes\mathbf{n}_1 + \mathbf{t}_2\otimes(-\cos\theta\mathbf{n}_1 + \sin\theta\mathbf{m}_1)\right] + \\
& \mu g\left[\left(\mathbf{t}_1^\mathsf{T}\mathbf{t}_2\right)\mathbf{t}_1\otimes\mathbf{m}_1 + \left(\mathbf{t}_2^\mathsf{T}\mathbf{t}_2\right)\mathbf{t}_2\otimes(-\sin 2\theta\mathbf{n}_1 - \cos 2\theta\mathbf{m}_1)\right] + \\
& \mu g\left(\mathbf{s}^\mathsf{T}\mathbf{t}_2\right)\left[\mathbf{s}\otimes\left(-\frac{1}{2}\sin 2\theta\mathbf{n}_1 + \sin^2\theta\mathbf{m}_1\right) + (\mathbf{t}_1 - \cos\theta\mathbf{t}_2)\otimes\mathbf{e}\right], \\
\mathbf{H}\boldsymbol{\zeta}_2 =& \mu p\sin\theta\left(\mathbf{t}_2^\mathsf{T}\mathbf{t}_2\right)\left(\mathbf{t}_1\otimes\mathbf{n}_1 + \mathbf{t}_2\otimes(-\cos\theta\mathbf{n}_1 + \sin\theta\mathbf{m}_1)\right) + \\
& \mu g\left[\left(\mathbf{t}_1^\mathsf{T}\mathbf{t}_2\right)\mathbf{t}_1\otimes\mathbf{n}_1 + \left(\mathbf{t}_2^\mathsf{T}\mathbf{t}_2\right)\mathbf{t}_2\otimes(-\cos 2\theta\mathbf{n}_1 + \sin 2\theta\mathbf{m}_1)\right] + \\
& \mu g\sin\theta\left(\mathbf{s}^\mathsf{T}\mathbf{t}_2\right)\left[\mathbf{s}\otimes(\sin\theta\mathbf{n}_1 + \cos\theta\mathbf{m}_1) + \mathbf{t}_2\otimes\mathbf{e}\right], \\
\mathbf{H}\boldsymbol{\zeta}_3 =& \mu p\sin\theta\left(\mathbf{t}_2^\mathsf{T}\mathbf{t}_1\right)\left(\mathbf{t}_1\otimes\mathbf{n}_1 + \mathbf{t}_2\otimes(-\cos\theta\mathbf{n}_1 + \sin\theta\mathbf{m}_1)\right) + \\
& \mu g\left[\left(\mathbf{t}_1^\mathsf{T}\mathbf{t}_1\right)\mathbf{t}_1\otimes\mathbf{n}_1 + \left(\mathbf{t}_2^\mathsf{T}\mathbf{t}_1\right)\mathbf{t}_2\otimes(-\cos 2\theta\mathbf{n}_1 + \sin 2\theta\mathbf{m}_1)\right] + \\
& \mu g\sin\theta\left(\mathbf{s}^\mathsf{T}\mathbf{t}_1\right)\left[\mathbf{s}\otimes(\sin\theta\mathbf{n}_1 + \cos\theta\mathbf{m}_1) + \mathbf{t}_2\otimes\mathbf{e}\right], \\
\mathbf{H}\boldsymbol{\zeta}_4 =& \mu p\left[\mathbf{t}_1^\mathsf{T}\mathbf{s} - \cos\theta\left(\mathbf{t}_2^\mathsf{T}\mathbf{s}\right)\right]\left[\mathbf{t}_1\otimes\mathbf{n}_1 + \mathbf{t}_2\otimes(-\cos\theta\mathbf{n}_1 + \sin\theta\mathbf{m}_1)\right] + \\
& \mu g\left[\left(\mathbf{t}_1^\mathsf{T}\mathbf{s}\right)\mathbf{t}_1\otimes\mathbf{m}_1 + \left(\mathbf{t}_2^\mathsf{T}\mathbf{s}\right)\mathbf{t}_2\otimes(-\sin 2\theta\mathbf{n}_1 - \cos 2\theta\mathbf{m}_1)\right] + \\
& \mu g\left(\mathbf{s}^\mathsf{T}\mathbf{s}\right)\left[\mathbf{s}\otimes\left(-\frac{1}{2}\sin 2\theta\mathbf{n}_1 + \sin^2\theta\mathbf{m}_1\right) + (\mathbf{t}_1 - \cos\theta\mathbf{t}_2)\otimes\mathbf{e}\right], \\
\mathbf{H}\boldsymbol{\zeta}_5 =& \mu p\sin\theta\left(\mathbf{t}_2^\mathsf{T}\mathbf{s}\right)\left(\mathbf{t}_1\otimes\mathbf{n}_1 + \mathbf{t}_2\otimes(-\cos\theta\mathbf{n}_1 + \sin\theta\mathbf{m}_1)\right) + \\
& \mu g\left[\left(\mathbf{t}_1^\mathsf{T}\mathbf{s}\right)\mathbf{t}_1\otimes\mathbf{n}_1 + \left(\mathbf{t}_2^\mathsf{T}\mathbf{s}\right)\mathbf{t}_2\otimes(-\cos 2\theta\mathbf{n}_1 + \sin 2\theta\mathbf{m}_1)\right] + \\
& \mu g\sin\theta\left(\mathbf{s}^\mathsf{T}\mathbf{s}\right)\left[\mathbf{s}\otimes(\sin\theta\mathbf{n}_1 + \cos\theta\mathbf{m}_1) + \mathbf{t}_2\otimes\mathbf{e}\right] \\
\mathbf{H}\boldsymbol{\zeta}_6 =& \mu g\left[\left(\mathbf{t}_1^\mathsf{T}\mathbf{t}_1\right)\mathbf{s}\otimes\mathbf{n}_1 + \left(\mathbf{t}_2^\mathsf{T}\mathbf{t}_1\right)\mathbf{s}\otimes(-\cos\theta\mathbf{n}_1 + \sin\theta\mathbf{m}_1)\right], \\
\mathbf{H}\boldsymbol{\zeta}_7 =& \mu g\left[\left(\mathbf{t}_1^\mathsf{T}\mathbf{t}_2\right)\mathbf{s}\otimes\mathbf{n}_1 + \left(\mathbf{t}_2^\mathsf{T}\mathbf{t}_2\right)\mathbf{s}\otimes(-\cos\theta\mathbf{n}_1 + \sin\theta\mathbf{m}_1)\right].
\end{aligned}$$